The Astrophysical Journal, 877:127 (23pp), 2019 June 1 https://doi.org/10.3847/1538-4357/ab141a

Open and Closed Magnetic Configurations of Twisted Flux Tubes

Samrat Sen and A. Mangalam
Indian Institute of Astrophysics, Sarjapur Road, Koramangala 2nd Block, Bangalore-560034, India; samrat@iiap.res.in, mangalam@iiap.res.in
Received 2018 December 13; revised 2019 March 22; accepted 2019 March 26; published 2019 June 3

Abstract

We construct two classes of magnetohydrostatic (MHS) equilibria for an axisymmetric vertical flux tube spanning from the photosphere to the lower part of the transition region within a realistic stratified solar atmosphere subject to solar gravity. We assume a general quadratic expression of the magnetic flux function for the gas pressure and poloidal current and solve the Grad–Shafranov equation analytically. The solution is a combination of a homogeneous and a particular part where the former is separable by a Coulomb function in r and exponential in z, while the particular part is an open configuration that has no z dependence. We also present another open field solution by using a self-similar formulation with two different profile functions and incorporating stratified solar gravity to maintain the magnetohydrostatic equilibria, which is a modification of earlier self-similar models with a twist. We study the admitted parameter space that is consistent with the conditions in the solar atmosphere and derive the magnetic and thermodynamic structures inside the flux tube that are reasonably consistent with the photospheric magnetic bright points for both open and closed field Coulomb function and self-similar models as estimated from observations and simulations. The obtained open and closed field flux tube solutions can be used as the background conditions for the numerical simulations for the study of the wave propagation through the flux tubes. The solutions can also be used to construct realistic magnetic canopies.

Key words: magnetohydrodynamics (MHD) – Sun: activity – Sun: magnetic fields – Sun: photosphere – Sun: transition region

1. Introduction

The small-scale magnetic structure in the solar photosphere plays an important role in several phenomena, such as the evolution of active regions (Muller & Mena 1987; Aschwanden et al. 2000; Centeno et al. 2007), heating of the corona through the dissipation of waves (Ruzmaikin & Berger 1998; Srivastava et al. 2017), and reconnection between flux tubes (van Ballegooijen 1986; Muller et al. 1994). Magnetic flux tubes span from the photosphere to the higher atmosphere and are observed in the form of small-scale magnetic structures. The topological rearrangement of these flux tubes due to the motion of the photospheric footpoints gives rise to magnetic reconnection, leading to energy release in the solar corona (Parker 1988; Peter et al. 2005; Thalmann et al. 2013). Therefore, modeling of the proverbial flux tube is a key aspect of understanding the various phenomena on the solar surface and the Sun's outer atmosphere.

There have been several previous attempts to construct a model of flux tubes for both twisted and untwisted magnetic fields. Schlüter & Temesváry (1958) studied a two-dimensional (2D) axisymmetric flux tube model without twist for sunspots using self-similar structure, where a self-similar parameter was defined as a combination of r and z, and the relative vertical magnetic field strength at any arbitrary point with respect to the magnetic field strength at the axis is scaled with a Gaussian profile function of the self-similar parameter. This model is valid for open field lines in which the magnetic lines of force rise from a horizontal plane and do not return in the model domain. Yun (1971) implemented a twist in the self-similar structure to model the sunspots. In this model, an empirical form of the azimuthal magnetic field strength $B_\phi(r, z)$ was taken from the data obtained from observations (Stepanov 1965). By solving for the variation of the pitch angle and gradient of the pitch angle, the thermodynamic quantities with the depth were calculated. Motivated by the model and the self-similar structure proposed by Schlüter & Temesváry (1958), Osherovitch (1982) assumed a quadratic form of the flux function for the gas pressure to model a closed field flux tube, where the magnetic lines of force rise and return to the same horizontal plane.

Steiner et al. (1986) numerically studied a 2D model of an open single flux tube with a twist using the standard boundary conditions (BCs) including sheet current to study the magnetic field line structure within and outside the flux tube. The magnetic and thermodynamic structure for both single and multiple flux tubes that span from the photosphere to the corona have been studied for the case of an untwisted magnetic field (Gent et al. 2013, 2014), in which an empirical form of the magnetic field components is motivated by a self-similar construction. A numerical model of flux tubes was studied by Murawski et al. (2015), where an empirical form of magnetic flux function was assumed; this was followed by a model to study the propagation of the MHD waves through flux tubes with an azimuthal velocity perturbation. The steady structure of the 2D flux tube was used as a background initial condition to study the propagation of the MHD waves. For example, Vigeesh et al. (2009) assumed an empirical form of gas pressure for investigating the wave propagation and energy transport through the flux tube. Other interesting results of wave behavior in the solar atmosphere have been presented by several authors. Fedun et al. (2009) studied the propagation of the acoustic wave through the solar atmosphere due to the periodic drivers at the photosphere, and Shelyag et al. (2010) modeled the wave propagation through the photospheric magnetic bright points (MBPs).

In this work, we have constructed two different models of flux tubes with twisted magnetic field for open and closed field lines by solving the Grad–Shafranov equation (GSE; Grad & Rubin 1958; Shafranov 1958). We have assumed a quadratic form of the flux function for the gas pressure and poloidal

current, which has previously been used to study the equilibrium solution of terrestrial plasma (Atanasiu et al. 2004), and we extend it to solar flux tubes. As the MHD waves follow the magnetic field lines, it is important to model flux tubes with open field lines, so that MHD waves propagate through the flux tube and dissipate in the upper atmosphere, which is a key aspect of the coronal heating. A main goal of this paper is to show that the closed field model, reported in Sen & Mangalam (2018; hereafter SM18), is a special case of the open field model with a twisted field line. The flux tube we build is axisymmetric in structure and spans vertically upward from the photosphere to the transition region. The case of a linear form of the flux function for the gas pressure and poloidal current, an equilibrium solution near the magnetic axis of a plasma torus, was reported by Solov'ev (1968). SM18 studied the homogeneous solution of GSE, which is a special case of the general solution of the quadratic case, to model a flux tube with closed field lines with a twist. Here, we present the full solution of the GSE, including both homogeneous and particular parts, to model a twisted open field flux tube. The other model we have built is a self-similar magnetic structure with twist, with a generalized Gaussian (or power law) incorporated into the magnetic shape functions; the gas pressure and poloidal current are taken to be quadratic functions of the flux function. The self-similar flux tube model expands with height, which spans from the photosphere to the transition region. After building the solutions semianalytically and applying appropriate BCs, we calculate the magnetic field structure and thermodynamic quantities inside the flux tube. As MBPs observed in the photosphere (Muller & Mena 1987; Centeno et al. 2007; Lagg et al. 2010; Shelyag et al. 2010) are likely to be flux tubes, we compare our model with the existing observations and simulations of MBPs.

The paper is organized as follows. In Section 2, we apply the GSE to the cylindrical flux tube case and describe the common BCs that are physically realistic and used in the modeling of our flux tubes. In Section 3, we present the Coulomb function model for open and closed fields, the appropriate BCs, and show how the open field Coulomb model generalizes the Coulomb field closed model. The solution of the self-similar model and the appropriate BCs are presented in Section 4. In Section 5, the results of our simulations and the variation of the magnetic and thermodynamic profile functions are presented for Coulomb function and self-similar models, and in Section 6, the results obtained from the models are applied to the existing observations of MBPs and the simulations for other solar flux tubes. In Section 7, we compare the Coulomb function and self-similar models and find the regime of validity; we also discuss the advancements we have made and how the models for open and closed field flux tubes are useful for building realistic structures. Finally, in Section 8, we summarize and highlight the major points of the work and conclude how our findings may be useful for future numerical studies. A glossary of all the symbols used throughout the paper is provided in Table 1.

2. GSE for the Cylindrical Flux Tube

In a magnetic medium of field strength $\boldsymbol{B}$, with gas (or plasma) pressure p and mass density ρ, the magnetohydrostatic (MHS) pressure balance equation is given by

$$-\nabla p + \frac{1}{4\pi}(\nabla \times \boldsymbol{B}) \times \boldsymbol{B} + \rho \boldsymbol{g} = 0, \tag{1}$$

where $\boldsymbol{g}$ denotes the acceleration due to gravity at the solar surface. The individual components of $\boldsymbol{B}$ can be expressed in terms of the poloidal flux function, $\Psi(r, z) = \int_0^r r' B_z(r', z) dr'$, in the following way:

$$B_r = -\frac{1}{r}\frac{\partial \Psi}{\partial z}; \quad B_z = \frac{1}{r}\frac{\partial \Psi}{\partial r}; \quad B_\phi = \frac{I_p}{r}, \tag{2}$$

where I_p represents the poloidal current. These forms of B_r, B_ϕ and B_z automatically ensure the solenoidal condition for $\boldsymbol{B}$. Using the axisymmetric condition we split the MHS equilibrium Equation (1) into the r- and z-directions and plug in the forms of magnetic field components from Equation (2), to find two scalar partial differential equations

$$\frac{\partial \Psi}{\partial r}\frac{\partial^2 \Psi}{\partial z^2} + \frac{\partial \Psi}{\partial r}\frac{\partial^2 \Psi}{\partial r^2} - \frac{1}{r}\left(\frac{\partial \Psi}{\partial r}\right)^2 + \frac{1}{2}\frac{\partial I_p^2}{\partial r} = -4\pi r^2 \frac{\partial p}{\partial r}, \tag{3a}$$

$$-\frac{\partial p}{\partial z} + \frac{1}{4\pi}\left[\frac{1}{r}\frac{\partial \Psi}{\partial z}\left(\frac{1}{r^2}\frac{\partial \Psi}{\partial r} - \frac{1}{r}\frac{\partial^2 \Psi}{\partial r^2}\right) - \frac{1}{r^2}\frac{\partial \Psi}{\partial z}\frac{\partial^2 \Psi}{\partial z^2} - \frac{1}{2r^2}\frac{\partial I_p^2}{\partial z}\right] - \rho g = 0, \tag{3b}$$

where we assume the form of the gas pressure to be

$$p(r, z) = p_1(\Psi) + p_2(z); \tag{4}$$

this form is required in order to have a non-zero density (see SM18). The ϕ part of Equation (1) gives $\nabla\Psi \times \nabla I_p = 0$, which implies $I_p = I_p(\Psi)$. We have the following form from Equations 3(a), (4) for the GSE to be given by:

$$\frac{\partial^2 \Psi}{\partial r^2} - \frac{1}{r}\frac{\partial \Psi}{\partial r} + \frac{\partial^2 \Psi}{\partial z^2} = -\frac{1}{2}\frac{\partial I_p^2(\Psi)}{\partial \Psi} - 4\pi r^2 \frac{\partial p_1(\Psi)}{\partial \Psi}. \tag{5}$$

From Equations 3(b), (4) we find

$$-\frac{\partial p_2}{\partial z} - \frac{\partial p_1(\Psi)}{\partial z} + \frac{1}{4\pi}\left[\frac{1}{r^2}\frac{\partial \Psi}{\partial z}\left(\frac{1}{r}\frac{\partial \Psi}{\partial r} - \frac{\partial^2 \Psi}{\partial r^2}\right) - \frac{1}{r^2}\frac{\partial \Psi}{\partial z}\frac{\partial^2 \Psi}{\partial z^2} - \frac{1}{2r^2}\frac{\partial I_p^2(\Psi)}{\partial z}\right] - \rho g = 0. \tag{6}$$

Following SM18, by multiplying $4\pi r^2 \frac{\partial z}{\partial \Psi}$ on both sides of Equation (6) and using Equation (5), we obtain

$$\rho(z) = -\frac{1}{g}\frac{dp_2(z)}{dz}. \tag{7}$$

We will see later that the prescription of $p_2(z)$ will lead ρ to be a positive quantity, hence the density within the flux tube is independent of the radial distance r but varies with height z. The temperature, T, inside the flux tube is calculated by the ideal gas law according to the following form:

$$T(r, z) = \frac{\bar{\mu}\, p(r, z)}{R_g\, \rho(z)}, \tag{8}$$

Table 1
Glossary of Symbols Used in the Different Flux Tube Models

Symbols common to all the models			
r	Radial coordinate in cylindrical geometry	ϕ	Azimuthal coordinate in cylindrical geometry
z	Vertical coordinate in cylindrical geometry	B_r	Radial component of the magnetic field strength
B_ϕ	Azimuthal component of the magnetic field strength	B_z	Vertical component of the magnetic field strength
B_0	Magnetic field strength at the center of the flux tube	I_p	Poloidal current
Ψ	Total flux function	Ψ_b	Flux at the boundary
k	Scale factor of the pressure-scale height	p	Gas pressure
p_T	Total pressure inside flux tube	p_0	Gas pressure at the photosphere
p_e	Pressure outside the flux tube in the solar atmosphere	p_t	Pressure at the transition region
z_t	Height of the transition region from the photosphere	ρ	Gas density inside the flux tube
T	Temperature inside the flux tube	g	Acceleration due to gravity at the photosphere
R_g	Universal gas constant	μ_e	Effective molar mass
$\bar{\mu}$	Mean effective molar mass		
Coulomb function model			
a, α, b, β, κ	Parameters of the GSE	ψ_h	Homogeneous solution of GSE, same as ψ_C^C
s	Radial part of the homogeneous solution	Z	Vertical part of homogeneous solution
ψ_p	Particular solution of GSE	ψ_C^X	General Coulomb solution of the GSE
ψ_C^O	Coulomb function open field solution	ψ_C^C	Coulomb function closed field solution
j_ϕ	Sheet current along azimuthal direction at flux tube boundary	j_z	Sheet current along vertical direction at flux tube boundary
p_{20}	Gas pressure at the center of the flux tube	R	Radius of the flux tube
r_b	Cutoff radius inside the flux tube		
Self-similar model			
ξ	Self-similar parameter	D_X	Shape function of the flux function
B'_{z0}	Vertical gradient of magnetic field at the center of the flux tube	$\bar{\chi}$	Dimensionless twist parameter of the field lines
$\bar{f}$	Dimensionless shape function parameter	p_c	Gas pressure at the center of the flux tube
ψ_S^O	Self-similar open field flux	R_{90}	Radius of the flux tube where 90% of the flux is enclosed
Generalized Gaussian flux tube model			
ψ_G	Flux function	D_G	Shape function of the flux function
n_G	Power index of shape function profile	R_G	Radius of the flux tube
Power-law flux tube model			
ψ_P	Flux function	D_P	Shape function of the flux function
n_P	Power index of the shape function profile	R_P	Radius of the flux tube

where, $R_g = 8.314\,\mathrm{J\,mol^{-1}\,K^{-1}}$ represents the gas constant and

$$\bar{\mu} = \frac{1}{z_t}\int_0^{z_t} \mu_e(z)dz = 1.12 \tag{9}$$

is the mean effective molar mass from the photosphere to the transition region given by the empirical relation, $\mu_e(z) = 1.288\left[1 - 0.535\left(\frac{z}{2.152}\right)^3\right]$ (Solov'ev & Kirichek 2015), in the domain of $0 < z < 2.152$ Mm. The formularies of the derived functions for the Coulomb function helical flux tube model are summarized in the Table 6. In Sections 3 and 4, we reduce the GSE for different models of flux tubes with open or closed field line structures. A flowchart of the obtained solutions of the two different flux tube models is shown in Figure 1.

Before we solve for the various cylindrical structures, we discuss the BCs that are crucial to the models, applicable to both open and closed field flux tubes. The magnetic field lines that rise from a horizontal plane and do not return to the same plane within the domain of interest are called open field lines (see Figures 6, 12, 13). The field lines that rise and return to the same horizontal plane are called the closed field lines (see Figure 7). We take an idealized case in which the flux tube is embedded in a magnetic field free region where there is no current outside the flux tube. We apply the following standard BCs that have been used by several authors (e.g., Mangalam & Krishan 2000; Solov'ev & Kirichek 2015; Sen & Mangalam 2018): $[B_r(r = 0, z) = 0,\ B_\phi(r = 0, z) = 0]$, which implies that the magnetic field line is vertical at the axis of the flux tube. At the boundary, the radial component vanishes, i.e., $B_r(r = R, z) = 0$. We also use BCs for which the total pressure at the boundary of the flux tube matches with the external pressure and the radial average of the internal gas pressure at the transition region ($z = z_t$) is equal to p_t, where the pressure at the photosphere ($z = 0$) outside the flux tube is taken to be $p_0 = 1.228 \times 10^5\,\mathrm{dyne\,cm^{-2}}$ and at the transition region ($z_t = 2$ Mm), it is $p_t = 0.1488\,\mathrm{dyne\,cm^{-2}}$; these are taken from the Avrett–Loeser model (Avrett & Loeser 2008). We specify the appropriate BCs to model both the open and

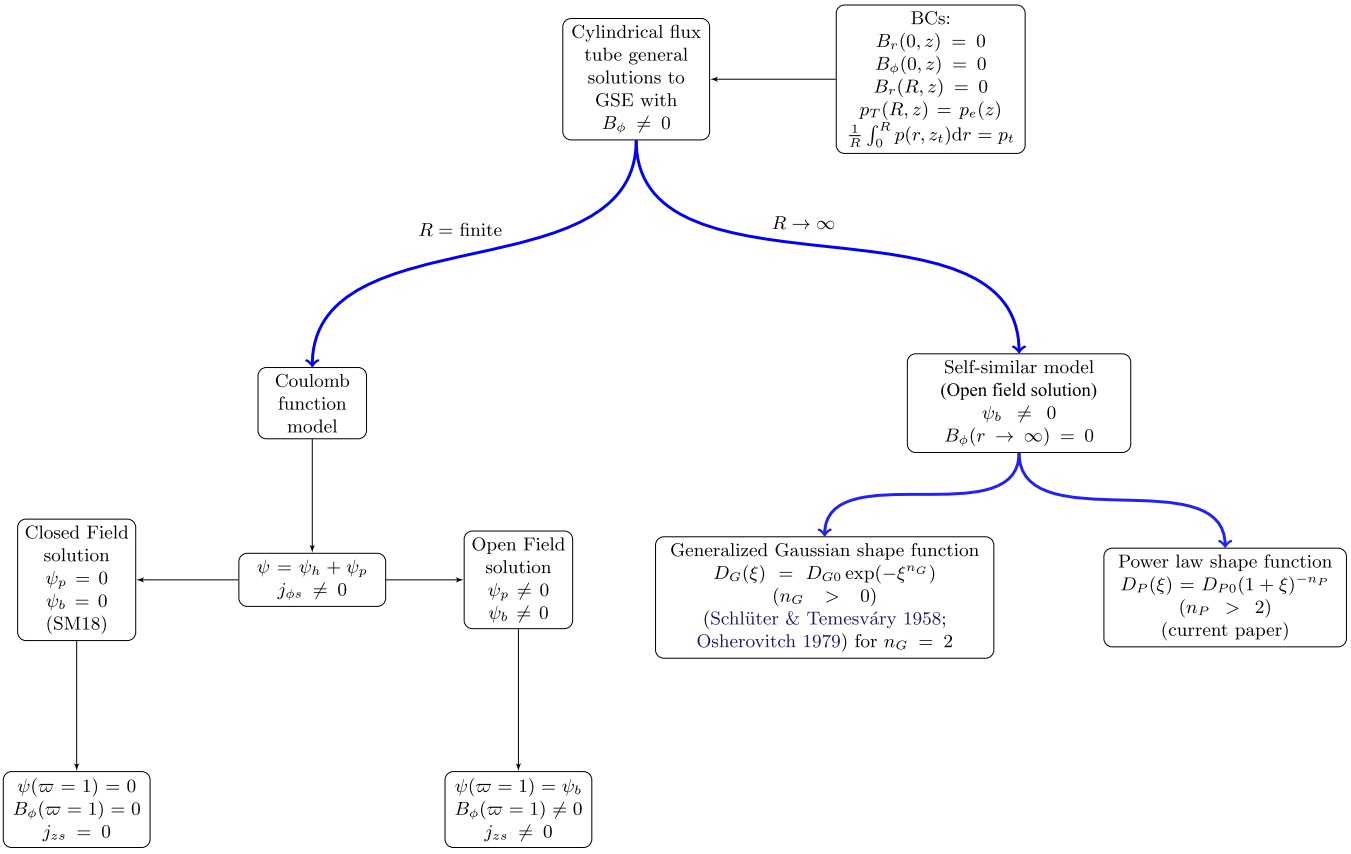

Figure 1. The two families of solutions presented in the text: the Coulomb function model and the self-similar model, shown along with the applicable boundary conditions.

closed field flux tubes below:

$$\text{BC1:} \quad B_r(r=0,z)=0, \tag{10a}$$

$$\text{BC2:} \quad B_\phi(r=0,z)=0, \tag{10b}$$

$$\text{BC3:} \quad B_r(R,z)=0, \tag{10c}$$

$$\text{BC4:} \quad p_T(R,z)=p_e(z), \tag{10d}$$

$$\text{BC5:} \quad \frac{1}{R}\int_0^R p(r,z_t)dr = p_t. \tag{10e}$$

The BCs that distinguish between the closed and open field flux tubes are as follows:

$$B_\phi(R,z)\begin{cases}=0; & \text{closedfield}\\ \neq 0; & \text{openfield},\end{cases} \tag{11}$$

which reduces to the condition,

$$\Psi(R,z)=\Psi_b\begin{cases}=0; & \text{closedfield}\\ \neq 0; & \text{openfield},\end{cases} \tag{12}$$

which is derived in Section 3. The open (general) solution is obtained in Section 3 and it is reduced to the special case of the closed solution by taking $\Psi_b = 0$, as presented in Section 3.

3. Coulomb Function Solution of the Helical Flux Tube Model

For magnetohydrostatic equilibria with uniform solar gravity and axisymmetric conditions, we have split $p(r,z) = p_1(\Psi(r,z)) + p_2(z)$ in order to have a non-zero density (SM18). If we take the form of $p_1(\Psi)$ as a linear function of Ψ, we find that BCs 1–5 (Equations 10(a)–(e)), which are crucial for our model, will not be satisfied for arbitrary R values. On the other hand, the quadratic function of Ψ, which is more general than the linear form, is the simplest allowed form for p_1 and I_p, satisfying all the BCs (Equations 10(a)–(e)), in which R becomes a free parameter, and can be can be any chosen value within the domain of our interest. Therefore, we assume $p_1(\Psi)$ and $I_p^2(\Psi)$ to be polynomials of Ψ up to second order (Atanasiu et al. 2004),

$$p_1(\Psi) = \frac{1}{4\pi}\left(\frac{a'}{2}\Psi^2 + b'\Psi\right), \tag{13a}$$

$$I_p^2(\Psi) = \alpha'\Psi^2 + 2\beta'\Psi + I_0^2, \tag{13b}$$

where the parameters a', b', α', β', I_0 are to be determined by appropriate BCs and the function $p_2(z)$ will be evaluated later. Plugging Equations 13(a), (b) into Equation (5) we obtain a second order scalar linear partial differential equation:

$$\frac{\partial^2\Psi}{\partial r^2} - \frac{1}{r}\frac{\partial\Psi}{\partial r} + \frac{\partial^2\Psi}{\partial z^2} = -(a'r^2 + \alpha')\Psi - (b'r^2 + \beta'). \tag{14}$$

We define the dimensionless parameters (on the LHS) by introducing the scaling relations,

$$\varpi = r/R,\ \ \tau = R/z_0,\ \ \psi_b = \frac{\Psi_b\sqrt{a'}}{B_0},\ \ a = \frac{a'R^4}{4},$$
$$\alpha = \frac{\alpha'}{4\sqrt{a'}},\ \ b = \frac{b'}{B_0\sqrt{a'}},\ \ \beta = \frac{R^2\beta'}{\Psi_b}, \tag{15}$$

where Ψ_b, R, B_0 are the boundary flux, radius and the magnetic field strength at the center of the flux tube, respectively, and $\bar{z} = z/z_0$, where z_0 is a constant. To solve this equation, we split $\psi = \Psi/\Psi_b$ into homogeneous ψ_h and particular part ψ_p, i.e., $\psi = \psi_h + \psi_p$. We plug ψ into Equation (14) and separate out the homogeneous and particular parts to obtain the following dimensionless equations:

$$\frac{\partial^2\psi_h}{\partial\varpi^2} - \frac{1}{\varpi}\frac{\partial\psi_h}{\partial\varpi} + \tau^2\frac{\partial^2\psi_h}{\partial\bar{z}^2} = -4\sqrt{a}\,(\sqrt{a}\,\varpi^2 + 2\alpha)\psi_h, \tag{16}$$

$$\frac{\partial^2\psi_p}{\partial\varpi^2} - \frac{1}{\varpi}\frac{\partial\psi_p}{\partial\varpi} = -(4a\varpi^2 + 8\sqrt{a}\,\alpha)\psi_p - \left(\frac{4ab}{\psi_b}\varpi^2 + \beta\right). \tag{17}$$

The solution of Equation (16) is separable and given by $\psi_h(\varpi, \bar{z}) = s(\varpi)Z(\bar{z})$, which has been shown in SM18 to be given by

$$s(\varpi) = cF_0(-\alpha - \kappa^2,\ \sqrt{a}\,\varpi^2) \qquad (\text{with } a > 0), \tag{18}$$

where $F_0(-\alpha - \kappa^2,\ \sqrt{a}\,\varpi^2)$ represents the Coulomb function (Abramowitz & Stegun 1972) and $\kappa = \frac{kR}{2\sqrt{2}\,a^{1/4}}$, where the value of k is evaluated later. The z-part solution of Equation (16) is given by

$$Z(\bar{z}) = \exp\left(-\frac{2\sqrt{2}\,\kappa a^{1/4}\bar{z}}{\tau}\right). \tag{19}$$

The homogeneous solution takes the following form:

$$\psi_h(\varpi, \bar{z}) = c\exp\left(-\frac{2\sqrt{2}\,\kappa a^{1/4}\bar{z}}{\tau}\right)F_0(-\alpha - \kappa^2,\ \sqrt{a}\,\varpi^2). \tag{20}$$

The solution of the inhomogeneous Equation (17) is given by a power=series solution

$$\psi_p(\varpi) = -\frac{\beta}{8\alpha} + \frac{i\sqrt{a}\,\varpi^2}{2}e^{-i\sqrt{a}\,\varpi^2}\left(\frac{\beta}{8\alpha} - \frac{b}{\psi_b}\right) \times \sum_{n=0}^{\infty}\frac{F_2^1\left(n+2,\,1;\,n+2+i\alpha;\,\frac{1}{2}\right)(i\sqrt{a}\,\varpi^2)^n}{(n+1+i\alpha)n!}. \tag{21}$$

A similar but different homogeneous solution that is oscillatory along the z-direction has been used for the cases of both D-shaped and toroidally diverted laboratory plasma (Atanasiu et al. 2004). The general solution of the GS Equation (14) is given by $\psi = \psi_h + \psi_p$. Since $\psi(\varpi, \bar{z})$ and $\psi^*(\varpi, \bar{z})$, its complex conjugate, are the valid solutions of Equation (14), we construct a real solution of Equation (14) by redefining $\frac{\psi_h(\varpi,\bar{z}) + \psi_h^*(\varpi,\bar{z})}{2} \to \psi_h(\varpi, \bar{z})$ and $\frac{\psi_p(\varpi) + \psi_p^*(\varpi)}{2} \to \psi_p(\varpi)$, which leads to

$$\frac{\psi(\varpi, \bar{z}) + \psi^*(\varpi, \bar{z})}{2} \to \psi(\varpi, \bar{z}) = \psi_C^X = \begin{cases}\psi_C^C = \psi_h & (\text{closed field})\\ \psi_C^O = \psi_h + \psi_p & (\text{open field})\end{cases}.$$

The solution ψ_h alone gives the closed field structure of the flux tube (SM18), which we denote as ψ_C^C; the general solution is a combination of ψ_h and ψ_p and we denote the open field flux tube structure as ψ_C^O.

The total flux function $\psi_C^X(\varpi, \bar{z})$ is given by

$$\psi_C^X(\varpi, \bar{z}) = s(\varpi)Z(\bar{z}) + \psi_p(\varpi), \tag{22}$$

where $s(\varpi)$ and $\psi_p(\varpi)$ are given by Equations (18) and (21), respectively. Now, $\psi_C^X(\varpi, \bar{z})$ has to be zero at the axis (i.e., $\varpi = 0$) for all $\bar{z}$, to keep the field finite at the origin. Since $s(0) = 0$, which satisfies the BC 1 (Equation 10(a)), we obtain from Equation (22), $\psi_p(\varpi = 0) = 0$. From Equation (21), we have $\psi_p(\varpi = 0) = -\frac{\beta}{8\alpha}$. Therefore, we obtain $\beta = 0$. From Equation (21), $\psi_p(\varpi)$ reduces to

$$\psi_p(\varpi) = \frac{i\sqrt{a}\,b\varpi^2}{4\psi_b} \times \left[e^{i\sqrt{a}\,\varpi^2}\sum_{n=0}^{\infty}\frac{F_2^1\left(n+2,\,1;\,n+2-i\alpha;\,\frac{1}{2}\right)(-i\sqrt{a}\,\varpi^2)^n}{(n+1-i\alpha)n!} - e^{-i\sqrt{a}\,\varpi^2}\sum_{n=0}^{\infty}\frac{F_2^1\left(n+2,\,1;\,n+2+i\alpha;\,\frac{1}{2}\right)(i\sqrt{a}\,\varpi^2)^n}{(n+1+i\alpha)n!}\right]. \tag{23}$$

From Equations (2) and (22) we have

$$B_z(\varpi, \bar{z}) = \frac{B_0 \psi_b}{2\sqrt{a}\,\varpi}\left(\frac{\partial \psi_h}{\partial \varpi} + \frac{\partial \psi_p}{\partial \varpi}\right), \tag{24}$$

and we obtain the explicit form for

$$\begin{aligned} B_z(\varpi, \bar{z}) &= \frac{B_0}{8\varpi} \\ &\times \left[\left\{1 - \frac{ib}{2}\left(\frac{F_2^1(1, -i\alpha, 2 - i\alpha, -1)}{1 - i\alpha}\right.\right.\right. \\ &\left.\left.\left. - \frac{F_2^1(1, i\alpha, 2 + i\alpha, -1)}{1 + i\alpha}\right)\right\} \\ &\cdot \exp\left(-\frac{2\sqrt{2}\,\kappa a^{1/4}\bar{z}}{\tau}\right)\frac{d}{d\varpi} \\ &[F_0(-\alpha - \kappa^2, \sqrt{a}\,\varpi^2) + F_0^*(-\alpha - \kappa^2, \sqrt{a}\,\varpi^2)] \\ &+ ib\frac{d}{d\varpi}\left\{\varpi^2 e^{i\sqrt{a}\,\varpi^2}\sum_{n=0}^{\infty}\right. \\ &\frac{F_2^1(n + 2, 1, n + 2 - i\alpha, 1/2)(-i\sqrt{a}\,\varpi^2)^n}{(n + 1 - i\alpha)n!} \\ &- \varpi^2 e^{-i\sqrt{a}\,\varpi^2}\sum_{n=0}^{\infty} \\ &\left.\left.\frac{F_2^1(n + 2, 1, n + 2 + i\alpha, 1/2)(-i\sqrt{a}\,\varpi^2)^n}{(n + 1 + i\alpha)n!}\right\}\right]. \end{aligned} \tag{25}$$

The steps to obtain Equation (25) are given in Appendix A. From Equations (2), (22) we have

$$B_r(\varpi, \bar{z}) = -\frac{B_0 \psi_b \tau}{2\sqrt{a}} s(\varpi) Z'(\bar{z}), \tag{26}$$

whose explicit form is given by

$$\begin{aligned} B_r(\varpi, \bar{z}) &= \frac{B_0 \kappa}{2\sqrt{2}\,a^{1/4}\varpi}\exp\left(\frac{-2\sqrt{2}\,\kappa a^{1/4}\bar{z}}{\tau}\right) \\ &\times [F_0(-\alpha - \kappa^2, \sqrt{a}\,\varpi^2) + F_0^*(-\alpha - \kappa^2, \sqrt{a}\,\varpi^2)] \\ &\cdot \left[1 - \frac{ib}{2}\left(\frac{F_2^1(1, -i\alpha, 2 - i\alpha, -1)}{1 - i\alpha}\right.\right. \\ &\left.\left. - \frac{F_2^1(1, i\alpha, 2 + i\alpha, -1)}{1 + i\alpha}\right)\right]. \end{aligned} \tag{27}$$

From Equation (2) we obtain the toroidal component

$$B_\phi(\varpi, \bar{z}) = \frac{\sqrt{2}\,B_0 \alpha^{1/2} \psi_b}{a^{1/4}\varpi}(\psi_h + \psi_p), \tag{28}$$

whose explicit form is given by

$$\begin{aligned} B_\phi(\varpi, \bar{z}) &= \frac{B_0 \alpha^{1/2} a^{-1/4}}{4\sqrt{2}} \\ &\times \left[\frac{1}{\varpi}\left\{1 - \frac{ib}{2}\left(\frac{F_2^1(1, -i\alpha, 2 - i\alpha, -1)}{1 - i\alpha}\right.\right.\right. \\ &\left.\left.\left. - \frac{F_2^1(1, i\alpha, 2 + i\alpha, -1)}{1 + i\alpha}\right)\right\} \\ &\cdot \exp\left(-\frac{-2\sqrt{2}\,\kappa\bar{z}}{\tau}\right) \\ &\times [F_0(-\alpha - \kappa^2, \sqrt{a}\,\varpi^2) + F_0^*(-\alpha - \kappa^2, \sqrt{a}\,\varpi^2)] \\ &+ ib\varpi\left\{e^{i\sqrt{a}\,\varpi^2}\sum_{n=0}^{\infty}\right. \\ &\frac{F_2^1(n + 2, 1, n + 2 - i\alpha, 1/2)(-i\sqrt{a}\,\varpi^2)^n}{(n + 1 - i\alpha)n!} \\ &- e^{-i\sqrt{a}\,\varpi^2}\sum_{n=0}^{\infty} \\ &\left.\left.\frac{F_2^1(n + 2, 1, n + 2 + i\alpha, 1/2)(-i\sqrt{a}\,\varpi^2)^n}{(n + 1 + i\alpha)n!}\right\}\right]. \end{aligned} \tag{29}$$

Applying BC 3 (Equation 10(c)) and using Equation (26), we find $s(\varpi = 1) = 0$. From BC 2 (Equations 10(b)) and 13(b) we find $I_0 = 0$. We assume that the external pressure from photosphere to transition region decreases exponentially as

$$p_e(z) = p_0 \exp(-2kz), \tag{30}$$

where k is the pressure-scale height, which is determined by the relation, $k = \frac{1}{2z_t}\ln\left(\frac{p_0}{p_t}\right) = 3.405\,\mathrm{Mm}^{-1}$, where $p_0 = 1.22 \times 10^5$ dyne cm^{-2}, $p_t = 0.148$ dyne cm^{-2}, and $z_t = 2$ Mm. By matching the pressure-scale heights inside and outside the flux tube, we see that $p_2(z)$ follows

$$p_2(z) = p_{20} \exp(-2kz), \tag{31}$$

where p_{20} is evaluated later. Finally, the expression of $p(r, z)$ from Equations (4), 13(a) is given by

$$p(r, z) = \frac{1}{4\pi}\left(\frac{a'}{2}\Psi^2 + b'\Psi\right) + p_{20}\exp(-2kz), \tag{32}$$

whose explicit form is given by

$$\begin{aligned} p(\varpi, \bar{z}) = B_0^2\left[\left(\frac{\psi_b^2 s^2(\varpi)}{8\pi} + \bar{p}_{20}\right)Z^2(\bar{z})\right. \\ + \left(\frac{\psi_b^2 s(\varpi)\psi_p(\varpi)}{4\pi} + \frac{b\psi_b s(\varpi)}{2\sqrt{2a}}\right)Z(\bar{z}) \\ \left. + \left(\frac{\psi_b^2 \psi_p^2}{8\pi} + \frac{b\psi_b\psi_p}{2\sqrt{2a}}\right)\right], \end{aligned} \tag{33}$$

where $\bar{p}_{20} = p_{20}/B_0^2$, and $s(\varpi)$, $Z(\bar{z})$, $\psi_p(\varpi)$ are given by Equations (18), (19), (23), respectively. We now calculate the total pressure at the boundary of the flux tube that includes the contribution due to gas pressure and the magnetic forces due to the

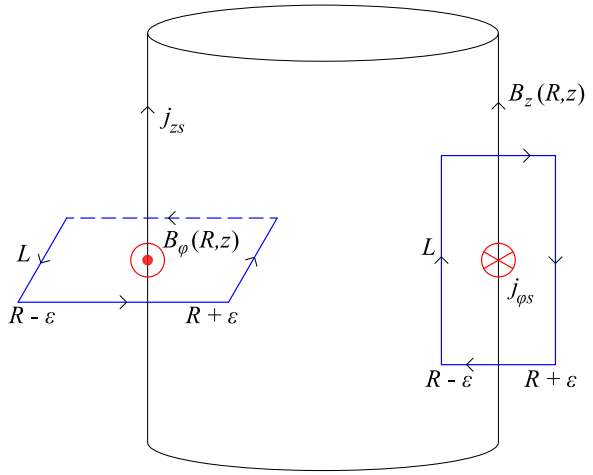

Figure 2. Geometry of the flux tube at the boundary showing sheet currents.

presence of the sheet currents j_ϕ (SM18) and j_z. The pressure and radial component of the MHS force balance Equation (1) yields

$$-\frac{\partial p}{\partial r}\bigg|_{r=R}+\frac{1}{4\pi}\left(B_r\frac{\partial B_r}{\partial r}+B_z\frac{\partial B_r}{\partial z}\right)\bigg|_{r=R}-\frac{\partial}{\partial r}\left(\frac{B^2}{8\pi}\right)\bigg|_{r=R}+j_\phi(R)B_z(R)-j_z(R)B_\phi(R)=0. \tag{34}$$

The sheet currents j_ϕ and j_z take the forms

$$j_\phi(r)=j_{\phi s}\ \delta(r-R), \tag{35a}$$

$$j_z(r)=j_{zs}\ \delta(r-R). \tag{35b}$$

Integrating Equation (34) with respect to r from $r=R-\epsilon$ to $r=R+\epsilon$ where ϵ is an infinitesimal positive quantity we obtain

$$-\int_{R-\epsilon}^{R+\epsilon}\frac{\partial p}{\partial r}dr+\frac{1}{4\pi}\left(\int_{R-\epsilon}^{R+\epsilon}B_r\frac{\partial B_r}{\partial r}dr+\int_{R-\epsilon}^{R+\epsilon}B_z\frac{\partial B_r}{\partial z}dr\right)-\int_{R-\epsilon}^{R+\epsilon}\frac{\partial}{\partial r}\left(\frac{B^2}{8\pi}\right)dr+\int_{R-\epsilon}^{R+\epsilon}j_\phi(r)B_z(r)dr-\int_{R-\epsilon}^{R+\epsilon}j_z(r)B_\phi(r)dr=0, \tag{36}$$

which leads to

$$p_i(R,z)-p_e(z)+j_{\phi s}\ B_z(R)-j_{zs}\ B_\phi(R)+\frac{1}{4\pi}\left[B_r\frac{\partial B_r}{\partial r}+B_z\frac{\partial B_r}{\partial z}\right]_R+\frac{B_i^2(R,z)-B_e^2(R,z)}{8\pi}=0, \tag{37}$$

where $[...]_R$ denotes the jump condition at the boundary and $\{B_i, p_i\}$ and $\{B_e, p_e\}$ are the internal and external magnetic fields and gas pressures in the flux tube, respectively. To calculate $j_{\phi s}$ and j_{zs}, we assume an infinitesimal current loop of vertical height L and radial extent $R-\epsilon$ to $R+\epsilon$ placed at the boundary of the flux tube (see Figure 2), and by applying the line integral along the loop, we obtain

$$B_z(R)L=4\pi L\int_{R-\epsilon}^{R+\epsilon}j_{\phi s}\delta(r-R)dr, \tag{38a}$$

$$-B_\phi(R)L=4\pi L\int_{R-\epsilon}^{R+\epsilon}j_{zs}\delta(r-R)dr, \tag{38b}$$

which implies

$$j_{\phi s}=\frac{B_z(R)}{4\pi} \tag{39a}$$

$$j_{zs}=-\frac{B_\phi(R)}{4\pi}. \tag{39b}$$

The total internal magnetic field is given by $B_i^2=B_r^2+B_\phi^2+B_z^2$. Applying the BC 3 (Equation 10(c)) and $B_e=0$, from Equation (37) we obtain

$$p_i(R,z)-p_e(z)+\frac{3B_z^2(R,z)}{8\pi}+\frac{3B_\phi^2(R,z)}{8\pi}=0. \tag{40}$$

By expanding Equation (40) we obtain

$$\frac{\psi_b^2}{3}\left(1+\frac{6\alpha}{\sqrt{a}}\right)+\frac{2}{3}b\psi_b+\frac{\psi_b^2}{4a}\times\left[\frac{1}{\varpi^2}\left(s'(\varpi)\exp\left(-\frac{2\sqrt{2}\,\kappa a^{1/4}\bar{z}}{\tau}\right)+\psi_p'(\varpi)\right)^2\right]_{\varpi=1}=\bar{p}\exp\left(-\frac{4\sqrt{2}\,\kappa a^{1/4}\bar{z}}{\tau}\right), \tag{41}$$

where $\psi_b=\psi_p(\varpi=1)$ and $\bar{p}=\frac{8\pi(p_0-p_{20})}{3B_0^2}$. By equating the coefficients of $\exp\left(-\frac{2\sqrt{2}\,\kappa a^{1/4}\bar{z}}{\tau}\right)$, $\exp\left(-\frac{4\sqrt{2}\,\kappa a^{1/4}\bar{z}}{\tau}\right)$ and the constant quantity between both sides of Equation (41), we obtain

$$\left(\frac{1}{\varpi^2}s'(\varpi)\psi_p'(\varpi)\right)_{\varpi=1}=0, \tag{42a}$$

$$\frac{\psi_b^2}{4a}\left(\frac{s'^2(\varpi)}{\varpi^2}\right)_{\varpi=1}=\bar{p}, \tag{42b}$$

$$\frac{\psi_b^2}{3}\left(1+\frac{6\alpha}{\sqrt{a}}\right)+\frac{2b\psi_b}{3}+\frac{\psi_b^2}{4a}\left[\frac{\psi_p'^2(\varpi)}{\varpi^2}\right]_{\varpi=1}=0. \tag{42c}$$

From Equations 42(a), 42(b) we find that $\left(\frac{\psi_p'(\varpi)}{\varpi}\right)_{\varpi=1}=0$, as $\bar{p}\neq 0$, hence, from Equation 42(c),

$$b=-\frac{\psi_b}{2}\left(1+\frac{6\alpha}{\sqrt{a}}\right). \tag{43}$$

We summarize the set of equations we need to solve numerically for the open field model as follows:

$$s(\varpi=1)=0, \tag{44a}$$

$$\left(\frac{\psi_p'(\varpi)}{\varpi}\right)_{\varpi=1}=0, \tag{44b}$$

$$\left(\frac{s'^2(\varpi)}{\varpi^2}\right)_{\varpi=1}=\frac{4a\bar{p}}{\psi_b^2}, \tag{44c}$$

$$b=-\frac{\psi_b}{2}\left(1+\frac{6\alpha}{\sqrt{a}}\right), \tag{44d}$$

Table 2
Expression of the Integrals in Equation (59) and λ_X in Equation (60), for Generalized Gaussian ($X = G$), and Power-law ($X = P$) Shape Function, Equation (57)

Functions	Shape Function $D_G(\xi)$ $(n_G > 0)$	Shape Function $D_P(\xi)$ $(n_P > 2)$
$\int_0^\infty \xi D_X^2(\xi) d\xi$	$\frac{n_G}{\Gamma(2/n_G)2^{2/n_G}}$	$\frac{(n_P-1)(n_P-2)^2}{2(2n_P-1)}$
$\int_0^\infty \frac{1}{2\xi^2}\frac{d\bar{I}_p^2}{d\xi} d\xi$	$\frac{\bar{\chi}\psi_b^2 n_G}{2^{2/n_G}\tau^2\Gamma(2/n_G)}$	$\frac{\bar{\chi}\psi_b^2(n_P-2)^2(n_P-1)}{2\tau^2(2n_P-1)}$
$\int_0^\infty \frac{\partial \bar{p}_1}{\partial \xi} d\xi$	$\bar{f}\psi_b^2/2$	$\bar{f}\psi_b^2/2$
$\lambda_X(n)$	$2^{2/n_G-1}$	$\frac{2n_P-1}{n_P-2}$

$$\int_0^1 p(\varpi, \bar{z}_t) d\varpi = p_t. \tag{44e}$$

The explicit forms of Equations 44(a)–44(e) are given by Equations (79)–(83) in Appendix B. The five Equations (79)–(83) consist of seven unknown variables, $\{a, \alpha, b, \psi_b, \bar{p}, R, B_0\}$; so there is a unique solution to the Coulomb function open field model for a given pair of unknown variables. Equations (79) and (80) contain three variables, a, α, and R, and we use these two equations to obtain $a(R)$ and $\alpha(R)$. From Equation (83), we calculate $\psi_b(R, B_0, b)$ and then find $b(R, B_0)$ from Equation (82), and hence $\psi_b(R, B_0)$, and then evaluate $\bar{p}(R, B_0)$ from Equation (81). As a result, the complete solution for the open field flux tube depends only on R and B_0, which are the free parameters of the model. Per BC1–BC5 (Equations 10(a)–10(e)), which are used for the open field flux tube model, the magnetic field component at the boundary of the flux tube is given by

$$B_\phi(\varpi = 1, \bar{z}) = \frac{\sqrt{2\alpha} B_0 \psi_b^2}{a^{1/4}}. \tag{45}$$

If we demand additionally that $B_\phi(\varpi = 1, \bar{z}) = 0$, then from Equation 44(d), $\psi_b = 0$; also, Equation 44(d) gives $b = 0$. Therefore, from Equation (23) we obtain

$$\psi_p(\varpi) = 0. \tag{46}$$

This represents the solution of the homogeneous part ψ_h of GSE, which has been discussed in SM18, and is applicable for the closed field flux tube model. Therefore, we need to solve Equations 44(a), (c), (e), which are given in their explicit forms by Equations (79), (81), (83) (with $b = \psi_b = 0$), numerically to find the parameters a, α, and $\bar{p}$ in terms of $\{R, B_0\}$, which are the free parameters of the closed field model. The formularies of the derived functions for the Coulomb function helical flux tube model are summarized in Table 6. We discuss the various configurations of the Coulomb function open and closed field structure of flux tubes in Section 5.1.

4. Self-similar Model

The basic formulation of a self-similar model of a flux tube is based on Schlüter & Temesváry (1958; hereafter ST58). For an axially symmetric cylindrical geometry (r, ϕ, z), where ϕ is ignorable, the magnetic field components are given by Equation (2). The coordinates r and z are combined together into a new dimensionless variable ξ, which is called the self-similar parameter and as a consequence, the flux function Ψ can be expressed only as a function of ξ, i.e., $\Psi(r, z) = \Psi(\xi)$ (ST58). We define the dimensionless parameters (in the LHS) by introducing the scaling relations

$$\varpi = r/R, \quad \tau = R/z_0, \quad \psi = \Psi/\Psi_b, \quad \psi_b = \frac{\Psi_b}{B_0 z_0^2},$$
$$\bar{p}_1 = p_1/B_0^2, \quad \bar{I}_p = \frac{I_p}{B_0 R}, \quad \bar{\chi} = \chi z_0^2, \tag{47}$$

where, Ψ_b, R, B_0 are the boundary flux, radius, and magnetic field strength at the center of the flux tube, respectively, and $\bar{z} = z/z_0$, where z_0 is a constant length. From ST58, the self-similar parameter ξ is defined by

$$\xi = \zeta(\bar{z})\varpi, \tag{48}$$

which describes the radial size distribution of the flux tube with height from the base. Plugging in Equation (48), we can rewrite the GS Equation (5) in the form

$$\frac{\psi_b^2}{2\tau^2}\frac{d}{d\xi}\left(\frac{d\psi}{d\xi}\right)^2 \zeta'^2(\bar{z}) + \frac{\psi_b^2}{\tau^2}\frac{1}{\xi}\left(\frac{d\psi}{d\xi}\right)^2 \zeta'(\bar{z})\zeta''(\bar{z}) + \frac{\psi_b^2}{2\tau^4}\frac{d}{d\xi}\left(\frac{1}{\xi}\frac{d\psi}{d\xi}\right)^2 \zeta^4(\bar{z}) + \frac{1}{2\xi^2}\frac{d\bar{I}_p^2}{d\xi}\zeta^2 = -4\pi\frac{\partial \bar{p}_1}{\partial \xi}, \tag{49}$$

and the z-part of GS Equation 3(b) gives the expression of ρ, Equation (7), which is self-consistent for both the Coulomb function and self-similar models. We define a quantity that is called the magnetic shape function given by

$$D_X(\xi) = \frac{1}{\xi}\frac{d\psi}{d\xi}. \tag{50}$$

Plugging Equation (50) into Equation (49) we obtain

$$\frac{\psi_b^2}{\tau^2}\xi D_X^2(\xi)\zeta\zeta'' + \frac{\psi_b^2}{2\tau^2}\frac{d}{d\xi}[\xi^2 D_X^2(\xi)]\zeta'^2 + \frac{\psi_b^2}{2\tau^4}\frac{d}{d\xi}(D_X^2(\xi))\zeta^4 + \frac{1}{2\xi^2}\frac{d\bar{I}_p^2}{d\xi}\zeta^2 = -4\pi\frac{\partial \bar{p}_1}{\partial \xi}, \tag{51}$$

and integrating Equation (51) with respect to ξ from 0 to ∞ we write

$$\frac{\psi_b^2}{\tau^2}\zeta\zeta''\int_0^\infty \xi D_X^2(\xi) d\xi + \frac{\psi_b^2\zeta'^2}{2\tau^2}[\xi^2 D_X^2(\xi)]_{\xi=0}^\infty + \frac{\psi_b^2\zeta^4}{2\tau^4}[D_X^2(\infty) - D_X^2(0)] + \frac{\zeta^2}{2}\int_0^\infty \frac{1}{\xi^2}\frac{d\bar{I}_p^2}{d\xi} d\xi = -4\pi\int_0^\infty \frac{\partial \bar{p}_1}{\partial \xi} d\xi. \tag{52}$$

Following ST58, we define

$$y^2(\bar{z}) = \frac{\psi_b D_0}{\tau}\zeta^2(\bar{z}), \tag{53}$$

Table 3
Numerical Values of the Different Parameters Obtained from the Coulomb Function Open Field Flux Tube Model for Different Combinations of R and B_0 Are Shown; the Units of the Various Quantities Are in the Square Brackets at the Top

Run #	B_0 [kG]	R [km]	ψ_b [10^{-3}]	a	α [10^{-2}]	κ [10^{6}]	b [10^{-3}]	$\bar{p}$
*C*1	1	100	2.57	9.390	2.74	4.85	1.350	0.109
*C*2	1.2	100	2.22	9.390	2.74	4.85	1.170	0.105
*C*3	1.5	100	1.80	9.390	2.74	4.85	0.949	0.104
*C*4	1	120	1.92	9.388	2.54	6.99	1.008	0.159
*C*5	1.2	120	1.62	9.388	2.54	6.99	0.849	0.165
*C*6	1.5	120	1.31	9.388	2.54	6.99	0.692	0.163
*C*7	1	130	1.69	9.389	2.43	8.21	0.880	0.184
*C*8	1.2	130	1.42	9.389	2.43	8.21	0.744	0.181
*C*9	1.5	130	1.15	9.389	2.43	8.21	0.603	0.182
*C*10	1	140	1.50	9.383	2.31	9.52	0.783	0.205
*C*11	1.2	140	1.25	9.383	2.31	9.52	0.661	0.204
*C*12	1.5	140	1.00	9.383	2.31	9.52	0.535	0.208
*C*13	1	150	1.38	9.378	2.18	10.93	0.723	0.233
*C*14	1.2	150	1.16	9.378	2.18	10.93	0.606	0.235
*C*15	1.5	150	0.94	9.378	2.18	10.93	0.492	0.237
*C*16	1	160	1.31	9.388	1.98	12.43	0.665	0.276
*C*17	1.2	160	1.11	9.388	1.98	12.43	0.577	0.276
*C*18	1.5	160	0.89	9.388	1.98	12.43	0.465	0.279
*C*19	1	180	1.14	9.395	1.72	15.73	0.587	0.402
*C*20	1.2	180	0.96	9.395	1.72	15.73	0.497	0.407
*C*21	1.5	180	0.78	9.395	1.72	15.73	0.405	0.409

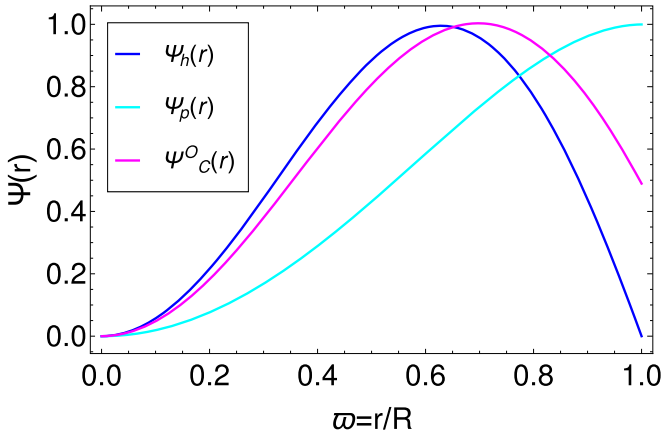

Figure 3. Radial variation of the flux function, normalized with respect to the maximum value, obtained from the Coulomb function open field model for run *C*4 in Table 3. The horizontal axis is scaled with respect to the total radius R.

where, $y(\bar{z}) \equiv \left(\frac{B_z(0,\bar{z})}{B_0}\right)^{1/2}$, $B_0 \equiv B_z(0, 0)$, and $D_0 \equiv D_X(\xi = 0)$. Next, using Equations (52) and (53), we obtain

$$\frac{\psi_b}{\tau}\frac{yy''}{D_0}\int_0^\infty \xi D_X^2(\xi)d\xi + \frac{\psi_b}{\tau}\frac{y'^2}{2D_0}[\xi^2 D_X^2(\xi)]_{\xi=0}^{\infty} + \frac{y^4}{2D_0^2\tau^2}[D_X^2(\infty) - D_0^2] + \frac{\tau}{\psi_b}\frac{y^2}{2D_0}\int_0^\infty \frac{1}{\xi^2}\frac{d\bar{I}_p^2}{d\xi}d\xi = -4\pi\int_0^\infty \frac{\partial\bar{p}_1}{\partial\xi}d\xi. \quad (54)$$

To solve Equation (54), we need to specify the functional form of p_1, I_p, and $D_X(\xi)$ to study the flux tube model with twisted magnetic field under the similarity assumption. The functional form of $p_1 = \frac{f}{2}\Psi^2$ is taken from Osherovitch (1982), where f is the shape function parameter, and the poloidal current, I_p, defined by Yun (1971) and Osherovitch (1979), and motivated from the observations of Stepanov (1965). Hence, the form of gas pressure p and poloidal current I_p are taken to be

$$p = p_c \exp(-2kz) + \frac{f}{2}\Psi^2, \quad (55)$$

$$I_p^2 = \Psi_b^2\chi\xi^4 D_X^2(\xi), \quad (56)$$

for the positivity of $\rho(z)$ at all z, which is given by Equation (7). Here, $p_2(z) = p_c \exp(-2kz)$ denotes the gas pressure at the flux tube axis, with p_c being the pressure at the center of the flux tube, and $\chi = \left(\frac{B_\phi}{rB_z}\right)^2$ being a constant pitch angle parameter. We deviate from (Yun 1971; Osherovitch 1982) by employing the extra term, $p_c \exp(-2kz)$, with p_1 in Equation (55), to maintain the hydrostatic vertical pressure balance condition under the influence of solar gravity, with two options for the shape function $D_X(\xi)$ specified by

$$D_X(\xi) = \begin{cases} D_G(\xi) = D_{G0}\exp(-\xi^{n_G}); & (n_G > 0): \text{ Generalized Gaussian} \\ D_P(\xi) = D_{P0}(1+\xi)^{-n_P}; & (n_P > 2): \text{ Power law} \end{cases} \quad (57)$$

where

$$D_{G0} = \frac{n_G}{\Gamma(2/n_G)}, \quad (58a)$$

$$D_{P0} = (n_P - 1)(n_P - 2). \quad (58b)$$

Table 4

Different Combinations of the Input Parameters and the Dimensionless Parameters for the Self-similar Model where R_G and R_P Represent the Radii of the Flux Tubes for the Generalized Gaussian and Power-law Profiles, Respectively

Run #	Ψ_b (10^{17} Mx)	B_0 (kG)	p_c (10^5 dyne cm^{-2})	B'_{z0} (G km^{-1})	χ (cm^{-2})	f (10^{-30} cm^{-4})	n_G	n_P	ψ_b	$\bar{f}$	$\bar{B}'_{z0}$	$\bar{\chi}$	R_G (km)	R_P (km)
*S*1	1	1	1	1	10^{-16}	4.56	2	3	0.01	456	1	1	214	261
*S*2	1	1	1	1	10^{-14}	4.56	2	3	0.01	456	1	100	214	261
*S*3	1	1	0.8	1.5	10^{-18}	8.56	2.5	3.5	0.01	856	1.5	0.01	196	138
*S*4	1	1	0.5	2	10^{-16}	14.56	3	4	1	1456	2	1	186	100
*S*5	1	2	1	1	10^{-14}	4.56	2	3	0.005	456	0.5	100	151	184
*S*6	1	2	0.8	1.5	10^{-18}	8.56	2.5	3.5	0.005	856	0.75	0.01	139	98
*S*7	1	2	0.5	2	10^{-16}	14.56	3	4	0.005	1456	0.25	1	131	71
*S*8	5	1	1	1	10^{-14}	0.182	2	3	0.005	18.2	1	100	479	584
*S*9	5	1	0.8	1.5	10^{-18}	0.342	2.5	3.5	0.005	34.2	1.5	0.01	439	308
*S*10	5	1	0.5	2	10^{-16}	0.582	3	4	0.005	58.2	2	1	416	225
*S*11	5	2	1	1	10^{-14}	0.182	2	3	0.025	18.2	0.5	100	339	413
*S*12	5	2	0.8	1.5	10^{-18}	0.342	2.5	3.5	0.025	34.2	0.75	0.01	310	218
*S*13	5	2	0.5	2	10^{-16}	0.582	3	4	0.025	58.2	0.25	1	294	159
*S*14	10	1	1	1	10^{-14}	0.0456	2	3	0.1	4.56	1	100	678	826
*S*15	10	1	0.8	1.5	10^{-18}	0.0856	2.5	3.5	0.1	8.56	1.5	0.01	621	436
*S*16	10	1	0.5	2	10^{-16}	0.145	3	4	0.1	14.56	2	1	589	318
*S*17	10	2	1	1	10^{-14}	0.0456	2	3	0.05	4.56	0.5	100	479	584
*S*18	10	2	0.8	1.5	10^{-18}	0.0856	2.5	3.5	0.05	8.56	0.75	0.01	439	308
*S*19	10	2	2	0.5	10^{-16}	0.145	3	4	0.05	14.56	0.25	1	416	225

Table 5

The Values of the Magnetic Field Strength and Thermodynamic Quantities Obtained from the Coulomb Function Open Field Flux Tube Model for the Parameter Set of Run *C*4 in Table 3, where $r_b = 84$ km; and the Self-similar Model with Gaussian Profile, where $R_G = 214$ km, and Power-law Profile, with $n_P = 3$, where $R_P = 261$ km, for the Parameter Set of Run *S*1 Corresponding to Table 4, Are Shown

Models	r	z (Mm)	B_z(G)	p (dyne cm^{-2})	ρ (g cm^{-3})	T (K)
Coulomb function open field	0	0	1000	1.030×10^5	2.44×10^{-7}	5656
	0	2	2.61	0.234	5.56×10^{-13}	5656
	r_b	0	0	1.04×10^5	2.44×10^{-7}	5690
	r_b	2	0	0.2445	5.56×10^{-13}	5890
Generalized Gaussian	0	0	10^3	1.0×10^5	2.37×10^{-7}	5630
	0	2	3.44	0.227	5.44×10^{-13}	5630
	R_G	0	6.73	1.17×10^5	2.37×10^{-7}	6620
	R_G	2	2.2	1.54	5.44×10^{-13}	38000
Power law	0	0	10^3	1.0×10^5	2.37×10^{-7}	5630
	0	2	75	0.227	5.44×10^{-13}	5630
	R_P	0	50	1.17×10^5	2.37×10^{-7}	6620
	R_P	2	19	1.75	5.44×10^{-13}	43000

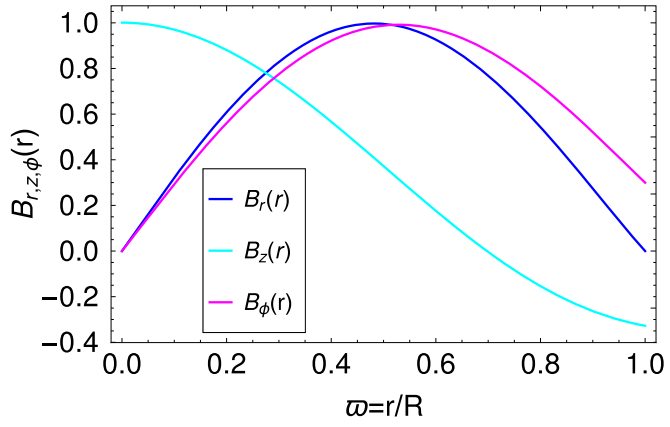

Figure 4. Radial variation of B_r, B_ϕ, and B_z, normalized with respect to the maximum values of $|B_r|$, $|B_\phi|$ and $|B_z|$, respectively, obtained from the Coulomb function open field model, for run *C*4 in Table 3. The horizontal axis is scaled with respect to the total radius *R*.

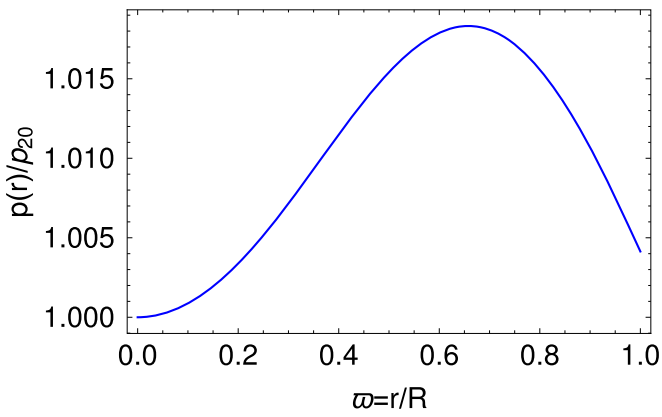

Figure 5. Radial variation of p normalized with the value at the center of the flux tube p_{20}, obtained from the Coulomb function open field model, for run *C*4 in Table 3. The horizontal axis is scaled with the total radius *R*.

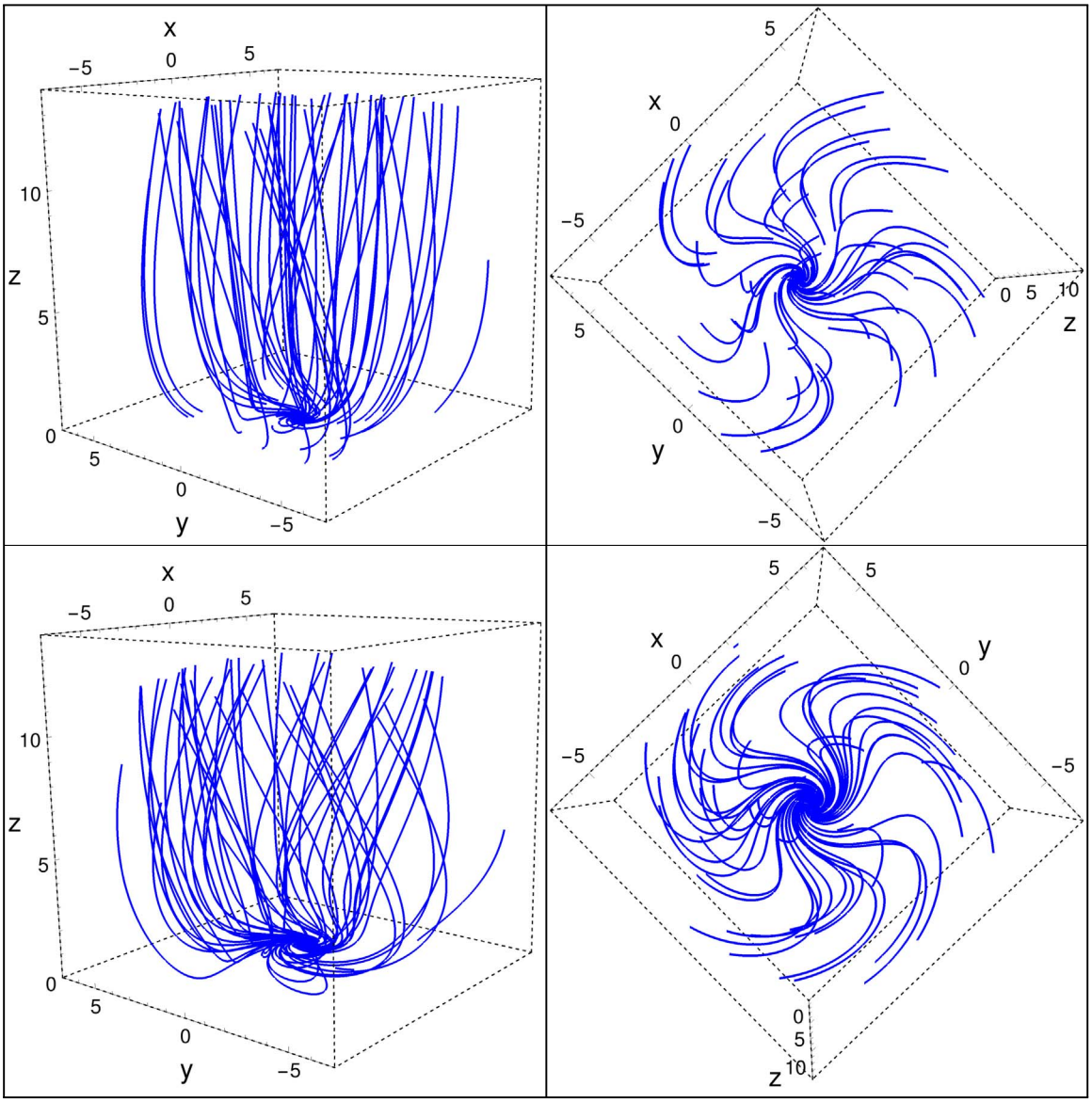

Figure 6. The 3D configuration of 50 different magnetic field lines for the open field flux tube obtained from the Coulomb function helical flux tube model. The left and right columns show the side and top views of the configuration. The domain of the simulation box is $-7 \leqslant x \leqslant 7$, $-7 \leqslant y \leqslant 7$, where the x- and y-axes are scaled in units of 20 km. The vertical domain is $0 \leqslant z \leqslant 14$ where the z-axis is scaled in units of 150 km. The field line configurations for the bottom and top rows are simulated for the parameter sets of runs $C4$ and $C10$, respectively, in Table 3.

We see that both the shape functions (Equation (57)) vanish asymptotically at $\xi \rightarrow \infty$; hence from Equation (54) we obtain

$$\frac{\psi_b}{\tau}\frac{yy''}{D_0}\int_0^\infty \xi D_X^2(\xi)d\xi - \frac{y^4}{2\tau^2} + \frac{\tau}{\psi_b}\frac{y^2}{D_0}\int_0^\infty \frac{1}{2\xi^2}\frac{d\bar{I}_p^2}{d\xi}d\xi = -4\pi\int_0^\infty \frac{\partial \bar{p}_1}{\partial \xi}d\xi. \quad (59)$$

Next, we evaluate the integrals of Equation (59) for both generalized Gaussian and power-law shape functions. We will see later that, from Equation (66), the flux function $\psi_P(\xi)$ varies as ξ^{2-n_P}, in the domain $0 < \xi < \infty$; therefore $\psi_P(\xi)$ will converge to a finite value at $\xi \rightarrow \infty$, if $n_p > 2$. The results of the integrals are provided in Table 2.

Using the values of the integrals from Table 2 and redefining $y'(\bar{z} = 0) \equiv y_0'$, we reduce Equation (59) to the form

$$\frac{dy}{d\bar{z}} = \left[\frac{\lambda_X(n)}{2\psi_b\tau}(y^4 - 1) - 2\bar{\chi}(y^2 - 1) - 8\pi\psi_b\bar{f}\,\lambda_X(n)\tau\ln(y) + \frac{\bar{B}'^2_{z0}}{4}\right]^{1/2}, \quad (60)$$

in which $\bar{B}'_{z0} = \frac{B'_{z0}z_0}{B_0}$, $\bar{\chi} = \chi z_0^2$, and $\bar{f} = fz_0^4$. The form of Equation (60) is common for both generalized Gaussian ($X = G$) and power-law ($X = P$) shape functions, where the functions $\lambda_X(n)$ for both shape functions are defined in Table 2. Here we have used the notation $B'_{z0} = B'_z(0, 0)$, which represents the vertical gradient of $B_z(0, z)$ at the center. From

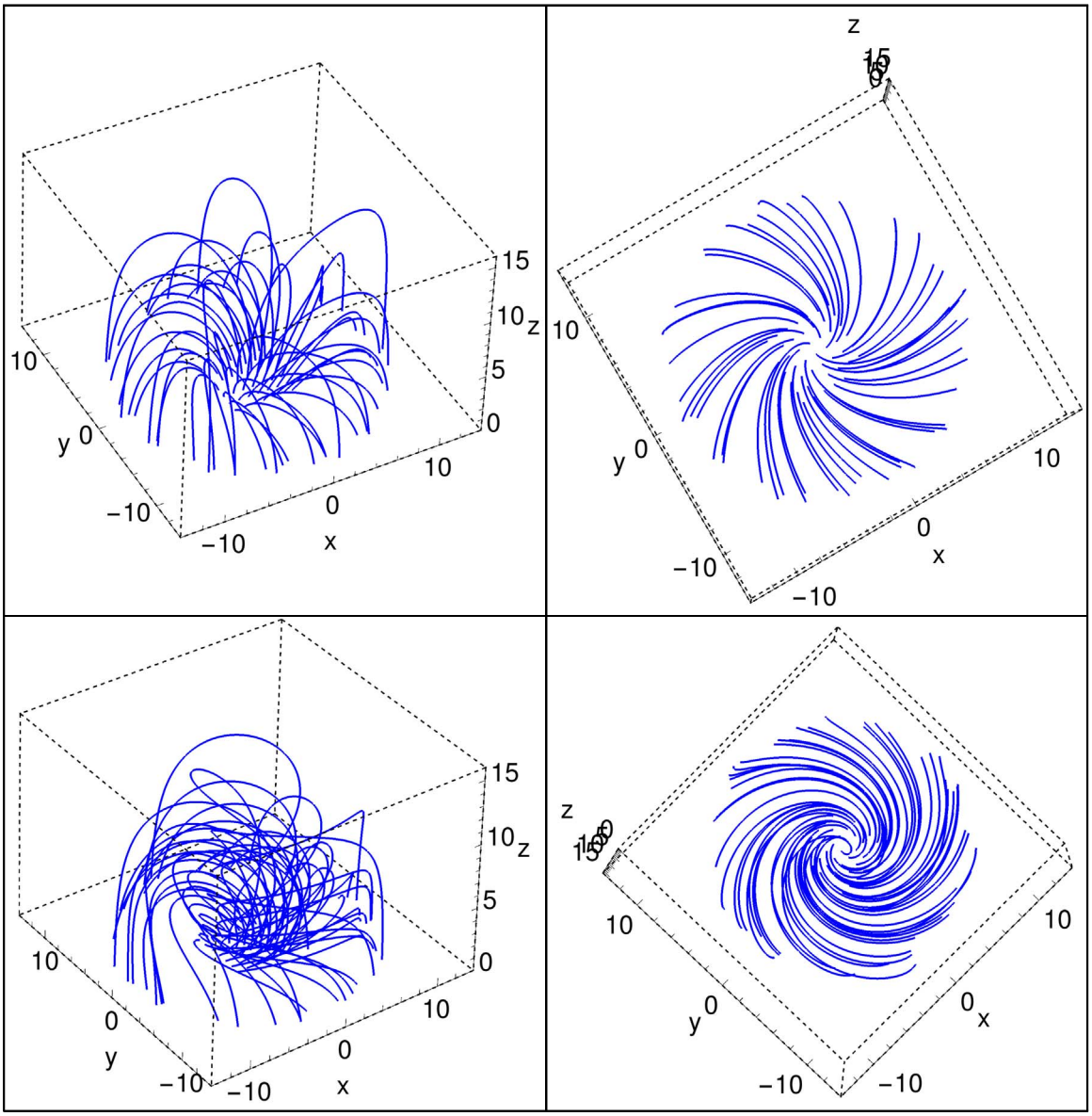

Figure 7. The 3D configuration of 50 different magnetic field lines for the closed field flux tube obtained from the Coulomb function helical flux tube model. The left and right columns show the side and top views of the configuration. The domain of the simulation box is $-14 \leqslant x \leqslant 14$, $-14 \leqslant y \leqslant 14$, where the x- and y-axes are scaled in units of 10 km. The vertical domain is $0 \leqslant z \leqslant 15$, where the z-axis is scaled in units of 150 km. The field line configurations for the bottom and the top rows are simulated for the parameter sets of runs $C4$ and $C10$, respectively, in Table 3.

Equation (60), we have the following integral relation:

$$\bar{z}(y) = \int_1^y \frac{dy'}{G(y')}, \tag{61}$$

where the function $G(y)$ is given by

$$G(y) = \left[\frac{\lambda_X(n)}{2\psi_b\tau}(y^4 - 1) - 2\bar{\chi}(y^2 - 1) - 8\pi\psi_b\bar{f}\,\lambda_X(n)\tau\ln(y) + \frac{\bar{B}'^2_{z0}}{4}\right]^{1/2}. \tag{62}$$

We evaluate the integral (61) numerically, which gives $\bar{z} = \bar{z}(y)$. Thereafter, inverting the function between $\bar{z}$ and y, we evaluate $y = y(\bar{z})$. From Equations (48), (53) we obtain

$$\xi = \sqrt{\frac{\tau}{\psi_b D_0}}\,\varpi y(\bar{z}). \tag{63}$$

Using the similarity assumption, $B_z(r, z) = \frac{B_0\psi_b}{\tau}\zeta^2(z)D_X(\xi)$ (ST58), and Equations (2), (48), (63) we calculate the magnetic field components, representing the most general self-similar solution, to be,

$$B_z(\varpi, \bar{z}) = \frac{B_0}{D_0}y^2(\bar{z})D_X(\xi), \tag{64a}$$

$$B_r(\varpi, \bar{z}) = -\frac{B_0\varpi}{D_0}y(\bar{z})y'(\bar{z})D_X(\xi), \tag{64b}$$

$$B_\phi(\varpi, \bar{z}) = \frac{\sqrt{\bar{\chi}} B_0}{D_0} \varpi y^2(\bar{z}) D_X(\xi). \tag{64c}$$

The flux function for the self-similar model is obtained by integrating the shape function

$$\psi_S^O(\xi) = \int_0^\xi \xi' D_X(\xi') d\xi'. \tag{65}$$

Employing Equations (50), (57), we obtain the open flux function for generalized Gaussian, ψ_G, and power-law, ψ_P, models to be given by

$$\psi_S^O(\xi) = \begin{cases} \psi_G(\xi) = 1 - \dfrac{\Gamma(2/n_G, \xi^{n_G})}{\Gamma(2/n_G)}; & (n_G > 0): \quad \text{Generalized Gaussian} \\ \psi_P(\xi) = 1 - (1+\xi)^{1-n_P}(1 + \xi(n_P - 1)); & (n_P > 2): \quad \text{Power law.} \end{cases} \tag{66}$$

From Equation (66) it is seen that $\psi_G(\xi)$ and $\psi_P(\xi)$ converge to unity for $\xi \to \infty$. The structure of the self-similar model of a flux tube is that the magnetic field decreases asymptotically in the radial direction to zero at infinity. The flux tube does not have any sharp boundary that can make a partition with the external solar atmosphere. In other words, the self-similar flux tube is embedded in a continuous magnetic medium that has a maximum field strength at the base of the axis of the flux tube and the radius of the flux tube is infinity. We take the effective radius of the flux tube as the distance from the axis on the $z = 0$ plane, which makes a circular area where 90% of the total flux is enclosed. We refer to this radius as R_{90}. The total flux is zero at the axis and it increases asymptotically with r. The explicit forms of the magnetic field components, obtained from Equations 64(a), (b), (c), using Equations (57), 58(a), (b), (63), are

$$B_z(\varpi, \bar{z}) = \begin{cases} B_0 y^2(\bar{z}) \exp\left[-\left(\sqrt{\dfrac{\tau\Gamma(2/n_G)}{n_G \psi_b}} y(\bar{z})\varpi\right)^{n_G}\right], & (n_G > 0): \quad \text{Generalized Gaussian} \\ B_0 y^2(\bar{z})\left[1 + \sqrt{\dfrac{\tau}{(n_P-1)(n_P-2)\psi_b}} y(\bar{z})\varpi\right]^{-n_P}, & (n_P > 2): \quad \text{Power law} \end{cases} \tag{67}$$

$$B_r(\varpi, \bar{z}) = \begin{cases} -B_0 y(\bar{z}) y'(\bar{z}) \varpi \exp\left[-\left(\sqrt{\dfrac{\tau\Gamma(2/n_G)}{n_G \psi_b}} y(\bar{z})\varpi\right)^{n_G}\right], & (n_G > 0): \quad \text{Generalized Gaussian} \\ -B_0 y(\bar{z}) y'(\bar{z}) \varpi\left[1 + \sqrt{\dfrac{\tau}{(n_P-1)(n_P-2)\psi_b}} y(\bar{z})\varpi\right]^{-n_P}, & (n_P > 2): \quad \text{Power law} \end{cases} \tag{68}$$

$$B_\phi(\varpi, \bar{z}) = \begin{cases} B_0 \sqrt{\bar{\chi}} y^2(\bar{z}) \varpi \exp\left[-\left(\sqrt{\dfrac{\tau\Gamma(2/n_G)}{n_G \psi_b}} y(\bar{z})\varpi\right)^{n_G}\right], & (n_G > 0): \quad \text{Generalized Gaussian} \\ B_0 \sqrt{\bar{\chi}} y^2(\bar{z}) \varpi\left[1 + \sqrt{\dfrac{\tau}{(n_P-1)(n_P-2)\psi_b}} y(\bar{z})\varpi\right]^{-n_P}, & (n_P > 2): \quad \text{Power law.} \end{cases} \tag{69}$$

The magnetic field components $B_r(\varpi, \bar{z})$ and $B_\phi(\varpi, \bar{z})$ for the self-similar model follow the BCs (1, 2, 3; Equations 10(a), (b), (c)) for $R = \infty$. $B_z(\varpi, \bar{z})$ decreases monotonically with ϖ and converges to zero at infinity. The total pressure far from the flux tube axis is only due to the gas pressure p. We use BC 4 (Equation 10(d)) at $z = 0$, for $r \to \infty$, so

$$p(r \to \infty, 0) = p_0. \tag{70}$$

From Equation (66), we see that the flux function for both a generalized Gaussian and power law converges to unity at $\varpi \to \infty$, i.e.,

$$\psi_S^O(\varpi \to \infty) = 1. \tag{71}$$

Using Equations (55), (70), we obtain

$$\bar{f} = 2(\bar{p}_0 - \bar{p}_c), \tag{72}$$

and the explicit form of $p(\varpi, \bar{z})$ for both the generalized Gaussian and the power-law models is given by

$$p(\varpi, \bar{z}) = B_0^2\left(\frac{\bar{f}}{2}\psi^2 + \bar{p}_c e^{-2\bar{k}\bar{z}}\right), \tag{73}$$

where $\bar{p}_0 = p_0/B_0^2$ and $\bar{p}_c = p_c/B_0^2$. The formularies of the derived functions for the self-similar flux tube model are summarized in Table 6. A flowchart of the solutions to the Coulomb function and self-similar models is shown in Figure 1.

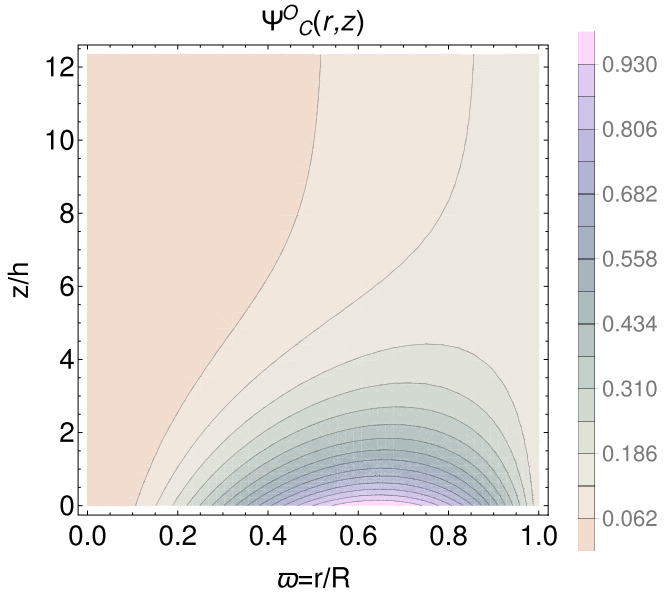

Figure 8. Contour plot of the flux function corresponding to run $C4$ in Table 3, obtained from the Coulomb function open flux tube model. The horizontal axis is scaled to the radius R and the vertical axis is scaled to the pressure-scale height $h = 162$ km. The contours have been normalized with respect to the maximum value of the flux function.

5. Results Obtained from the Models

5.1. Coulomb Function Helical Flux Tube Model

This magnetohydrostatic Coulomb function helical flux tube model consists of the free parameters R and B_0 and its functional dependence through $a(R)$, $\alpha(R)$, $\kappa(R)$, $b(R, B_0)$, $\psi_b(R, B_0)$, and $\bar{p}(R, B_0)$. We choose the parameter ranges, $1\,\mathrm{kG} \leqslant B_0 \leqslant 1.5\,\mathrm{kG}$ and $100\,\mathrm{km} \leqslant R \leqslant 180\,\mathrm{km}$, consistent with the observations of MBP size and field strength distributions (Utz et al. 2009, 2013). In Table 3, we show the solutions for combinations of the free parameters $\{R, B_0\}$, where we notice the following trends:

1. The boundary flux ψ_b decreases with R for the same B_0, and with B_0 for the same R within the parameter space of runs $C1 - C21$.
2. Due to the pressure balance at the boundary of the flux tube, $\bar{p}$ increases with R for the same B_0, but there is no fixed trend with B_0 for the same R within the parameter space of runs $C1 - C21$.

As an example, we show the solution of ψ_C^O, and the magnetic and thermodynamic structure of the flux tube for run $C4$. The radial variation of the solution of ψ_C^O, magnetic components, and pressure inside the flux tube are shown in Figures 3–5, respectively. Examples of 3D the configuration of the magnetic field lines for open and closed field are shown in Figures 6 and 7 for runs $C4$ and $C10$. A 2D vertical projection of the magnetic field lines for ψ_C^O inside the flux tube along $r - z$ plane is shown in Figure 8. The density inside the flux tube is constant along the radial direction, but it decreases along z, whereas the temperature varies along the r-direction and is nearly constant along the z-direction at the axis. The vertical variations of B_z, p, and ρ are shown in Figure 9. Conclusions from figures and tables are discussed in Section 7.

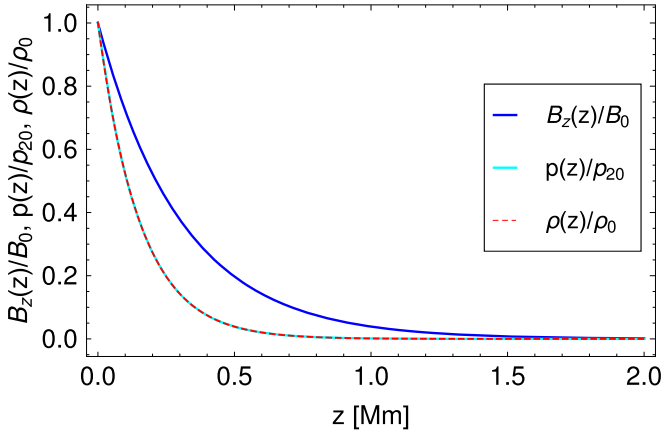

Figure 9. Vertical distribution of B_z, p, and ρ, normalized with respect to the values at the flux tube center, B_0, p_{20}, and ρ_0, respectively, obtained from Coulomb function open field model for the parameter set of run $C4$ in Table 3. The horizontal axis is scaled in the units of Mm. The values of the scale factors are $B_0 = 1$ kG, $p_{20} = 1.03 \times 10^5$ dyne cm^{-2} and $\rho_0 = 2.44 \times 10^{-7}$ g cm^{-3}.

5.2. Self-similar Model

The self-similar model we developed consists of the dimensionless parameters ψ_b, $\bar{B'}_{z0}$, $\bar{f}$, and $\bar{\chi}$, which are the functions of the input parameter set $\{\Psi_b, B_0, B'_{z0}, p_c, \chi\}$. The self-similar flux tube solutions are spanned by these parameters, but the structures remain similar. We use the values of these input parameters in the range, $\Psi_b = 10^{17}$–10^{18} Mx (Zhang et al. 1998; Hagenaar et al. 1999; Guglielmino et al. 2011), $B_0 = 1$–2 kG (Zhang et al. 1998), and B'_{z0} in the range 1–2 G km^{-1} (Wittmann 1974; Pahlke & Wiehr 1990; Balthasar & Schmidt 1993), $p_c < p_0$ (Shelyag et al. 2010 and SM18), which are observed for small-scale magnetic structures in the photosphere. The generalized Gaussian profile reduces to the Gaussian profile for $n_G = 2$, and it has been shown in Section 4 that for the power-law profile, the flux function converges to a finite value, at infinite radius, only for $n_P > 2$. We study the different cases for $n_G = 2$–3, $n_P = 3$–4 and $\bar{\chi} = 0.01$–100 for different combinations of the other parameter sets $\{\bar{\Psi}_b, \bar{B'}_{z0}, \bar{f}\}$, which are shown in runs $S1$–$S19$ of Table 4. For the parameter set of runs $S1$–$S19$, we find the following results:

1. For the same Ψ_b and B_0, with the increase of n_G and n_P, R_G and R_P decrease, respectively.
2. For the same n_G, n_P, and Ψ_b, with the increase of B_0, R_G and R_P decrease; whereas for the same n_G, n_P, and B_0, R_G and R_P increase with increasing Ψ_b.
3. For a fixed parameter set $\{\psi_b, \bar{B'}_{z0}\ \bar{f}, \bar{\chi}\}$, we see that $R_G > R_P$ for $n_G = 2$ and $n_P = 3$, but for values $n_G \geqslant 2.5$ and $n_P \geqslant 3.5$, $R_G < R_P$; this means that the radii of the flux tubes for the power-law profiles fall off more quickly than those of the generalized Gaussian profiles for higher values of n_G and n_P.

As an example, we show the solution of ψ_S^O and the magnetic and thermodynamic structures for run $S1$ in Table 4. The values of the magnetic and thermodynamic quantities obtained from the self-similar model are reported in Table 5, for both the Gaussian and power-law shape function profiles. The radial variations of the generalized Gaussian and power-law flux function are shown in Figure 10 for different values of n_G and n_P, and the variation along the $r - z$ plane is shown in

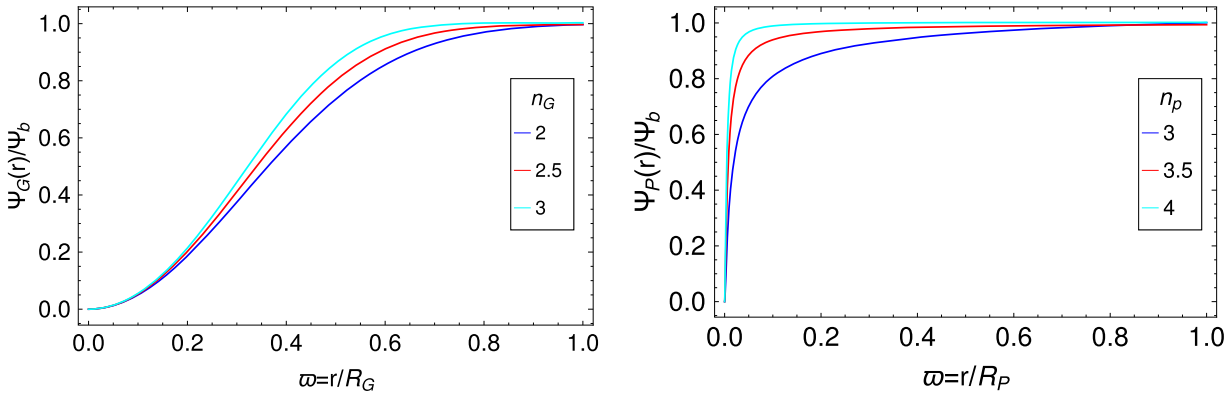

Figure 10. Radial variation of the flux function, normalized with respect to the maximum values for different values of n for generalized Gaussian (left) and power-law (right) shape functions for the parameter set of run $S1$ in Table 4. The horizontal axes are scaled with the total radius R.

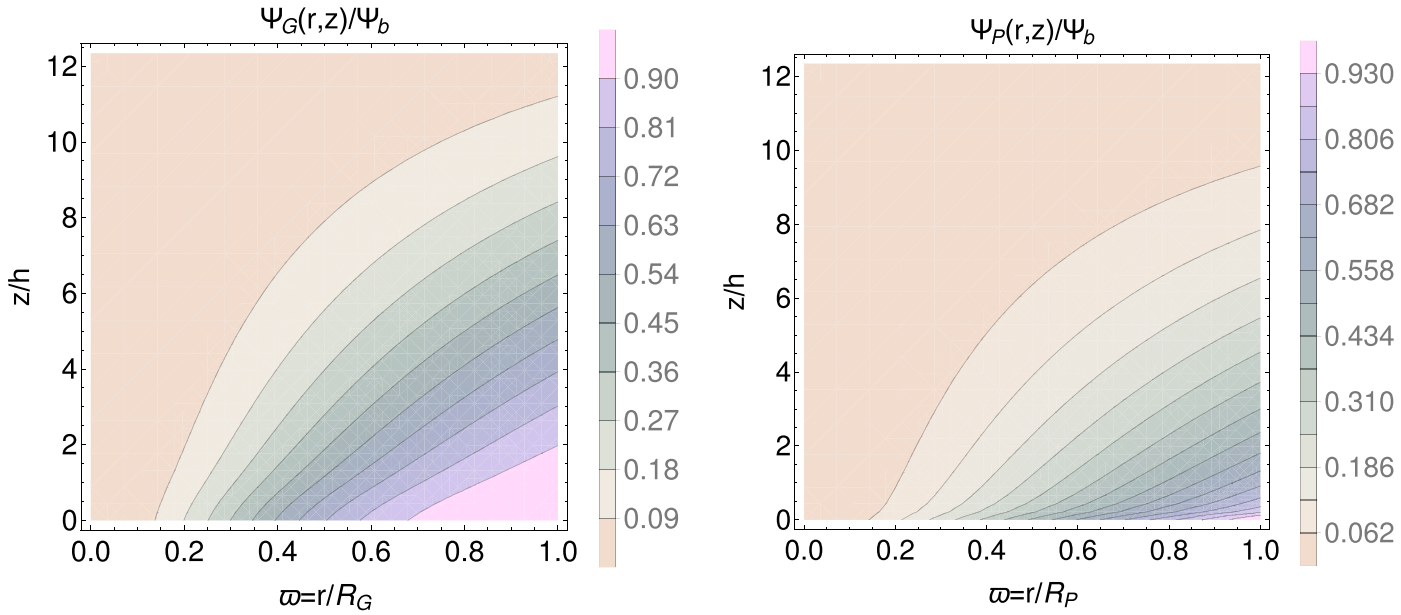

Figure 11. Contour plots of the flux functions for Gaussian (left) and power-law (right) profiles for $n_P = 3$ for the parameter set of run $S1$ in Table 4. The horizontal axes are scaled with the total radii $R_G = 214$ and $R_P = 261$ km, and the vertical axes are scaled with the pressure-scale height $h = 162$ km. The contours are normalized with respect to the maximum value of the flux function.

Figure 11. The 3D configurations of the field lines for the generalized Gaussian and power-law self-similar models are shown in the Figures 12 and 13 for the parameter sets for runs $S1$ and $S2$ given in Table 4. The radial and vertical distributions of the magnetic field components are shown in Figures 14 and 15, respectively, for both the Gaussian and power-law models, whereas the density inside the flux tube does not vary along the r-direction but decreases along the z-direction which is shown in the Figure 16. The variations of p and T in the $r - z$ plane obtained from the self-similar model are shown in Figures 19 and 20 for Gaussian and power-law shape function profiles. Conclusions drawn from Figures 6, 7, 9, 12, 13, 16, 18, 19, 20, 21, and Tables 3–5 are discussed in Section 7.

6. Comparing Our Models with Observations

We compare our models with the observations reported by high-resolution and high-cadence instruments. The small-scale magnetic structures in the solar photosphere are often found in the forms of MBPs, which are small-scale magnetic flux tubes with open field lines (Berger et al. 1995; Centeno et al. 2007; Lagg et al. 2010). Therefore, the MBPs are the best candidates to compare our open field flux tube models with the observations. MBPs can be identified by spectropolarimetric measurements or they can be seen by the G-band filtergrams (Utz et al. 2009, 2013; Yang et al. 2016). Next, we compare the observed magnetic field strength, size, and thermodynamic quantities of the MBPs with those obtained from our models. The MBPs are observed as a region of the unipolar flux concentration, therefore, in the Coulomb function model, we construct a cylindrical boundary of cutoff radius r_b inside the total simulation domain, where the line-of-sight magnetic field B_z vanishes. The magnetic field strength inside the cylinder of the cutoff radius is always positive. From the recent observations by Utz et al. (2009, 2013), it has been reported that the MBPs' number distribution for the size peaks in the range 160–200 km and the magnetic field strength is at ~1.4 kG. From Figure 4 we see that B_z vanishes at $r_b = 84$ km, where $R = 120$ km is the entire radial simulation domain. We choose the parameter ranges, $1\,\mathrm{kG} \leqslant B_0 \leqslant 1.5\,\mathrm{kG}$ and $100\,\mathrm{km} \leqslant R \leqslant 180\,\mathrm{km}$, for which the magnetic and thermodynamic quantities obtained from our model are in

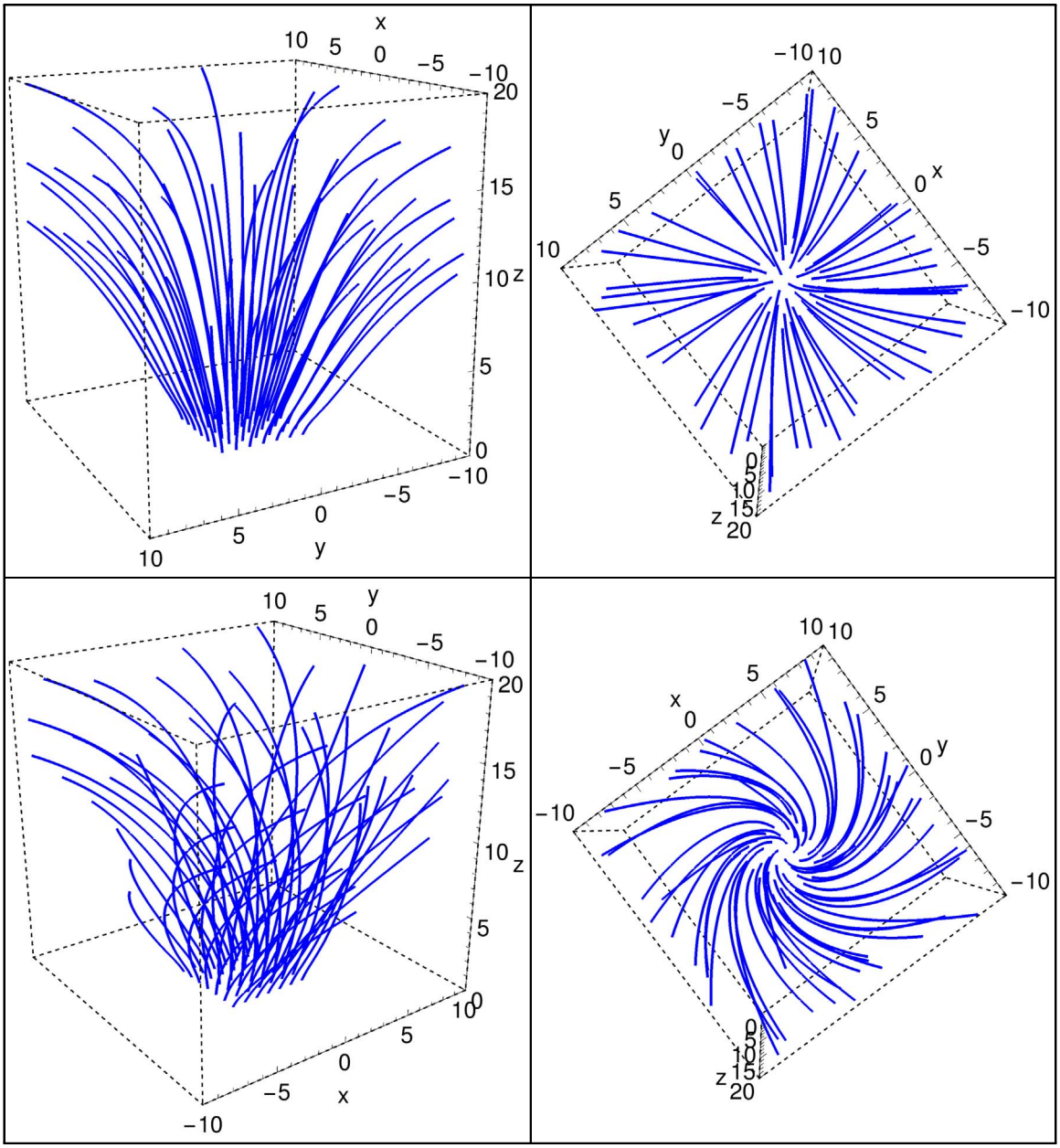

Figure 12. The 3D configuration of 50 different open field lines inside the flux tube obtained from the self-similar model for the Gaussian profile. The left and right columns show the side and the top views of the configurations, respectively. The domain of the simulation box is $-10 \leqslant x \leqslant 10$, $-10 \leqslant y \leqslant 10$ and $0 \leqslant z \leqslant 20$, where the x-, y-, and z-axes are scaled in units of 100 km. The field line configurations for the bottom and the top rows are simulated for the parameter values of Table 4 corresponding to runs $S1$ and $S2$, respectively.

reasonable agreement with the solar atmosphere (Vernazza et al. 1981), and the selection of the $\{R, B_0\}$ parameter space is also consistent with the observations of MBP size and field strength distributions (Utz et al. 2009, 2013). The values of the magnetic and thermodynamic quantities obtained from the Coulomb function open field model are reported in Table 5. For the self-similar model, the choice of the parameter space is consistent with the MBPs. We take the flux value in the range of 10^{17}–10^{18} Mx which is a typical flux value for MBPs(Zhang et al. 1998; Hagenaar et al. 1999; Guglielmino et al. 2011). According to previous studies by Shelyag et al. (2010) and SM18, the gas pressure at the axis of MBP is less than its boundary gas pressure, so we have chosen the parameter $p_c < p_0$. The field strengths of the magnetic footpoints observed in the photosphere for MBPs are $\sim$1 kG, with a distribution peak at 1.3 kG (Utz et al. 2013). Thus, we use the value of B_0 in the typical range of 1–2 kG (Zhang et al. 1998) in our model. The vertical gradient of the magnetic field strength at the photosphere is $\sim$1 G km^{-1} (Wittmann 1974; Pahlke & Wiehr 1990; Balthasar & Schmidt 1993). Hence, we use the value of $B_{z0}{}'$ in the range of 1–2 G km^{-1} in our model. We have reported combinations of the free parameters and the corresponding input parameters in Table 4. Within the parameter sets of runs $S1$–$S19$ in Table 4, we note that the minimum and maximum radii of the flux tubes are 151 and 678 km, respectively, for the Gaussian model, and 71 and 826 km, respectively, for the power-law model, which are in reasonable agreement with the observations of MBP size

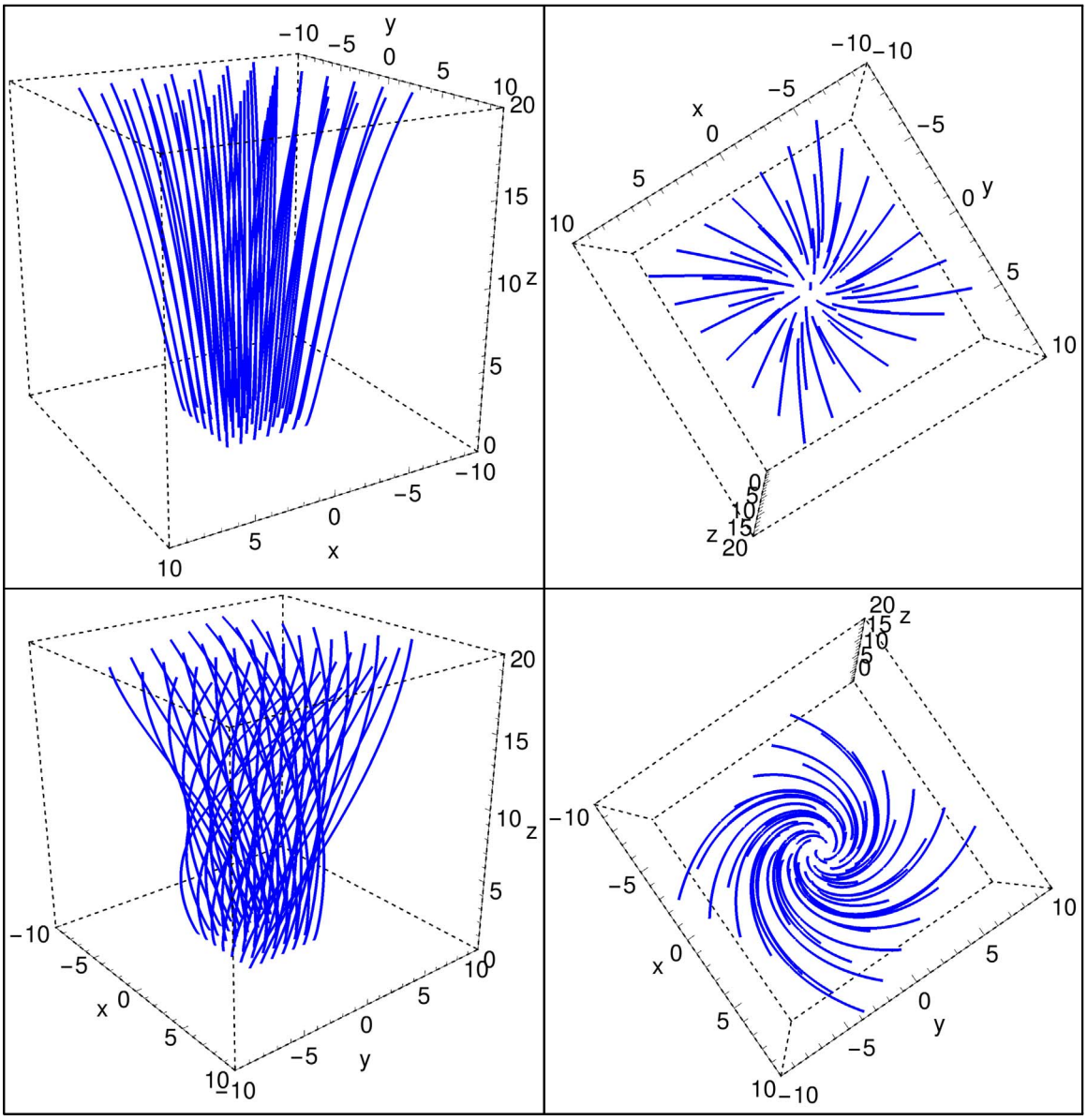

Figure 13. The 3D configuration of 50 different open field lines inside the flux tube obtained from the self-similar model for the power-law profile with $n_P = 3$. The left and right columns show the side and top views of the configurations. The domain of the simulation box is $-10 \leqslant x \leqslant 10$, $-10 \leqslant y \leqslant 10$ and $0 \leqslant z \leqslant 20$, where the x-, y-, and z-axes are scaled in units of 100 km. The field line configurations for the bottom and top rows are simulated for the parameter sets of runs *S*1 and *S*2, respectively, corresponding to Table 4.

distributions (Utz et al. 2009). The values of the magnetic and thermodynamic quantities obtained from a self-similar model are reported in Table 5, which is also in reasonable agreement with the solar atmosphere reported by Vernazza et al. (1981).

7. Discussion of the Models

The main findings of our simulations are as follows:

1. The Coulomb function model is easier to implement for the numerical studies, as it consists of two free parameters (R, B_0); on the other hand, the self-similar model consists of five free parameters (Ψ_b, B_0, p_c, B'_{z0}, and χ). From Table 5, we see that the rise of the gas pressure along the radial direction from the axis to the boundary is higher for the self-similar model than the Coulomb function model at higher z. The density within the flux tube does not vary with r; hence, the rise of the temperature from the axis to the boundary at higher z is also higher for the self-similar model relative to the Coulomb function model. For the Coulomb function model, the radial boundary of the flux tube is defined as where B_z vanishes; on the other hand, for the self-similar model, $B_z(R) \neq 0$, whereas B_z reduces along the radial direction from the axis to the boundary for the Gaussian model faster than it does for the power-law model.
2. The radial size and the magnetic field strength at the center of the flux tube are the free parameters in the Coulomb function model. The magnetic and thermodynamic structure of the flux tube remain similar for different values of the free parameters, whereas the magnitude of the magnetic and thermodynamic quantities vary. We have explored the parameter space and note that, in the domains of $100\,\mathrm{km} \leqslant R \leqslant 180\,\mathrm{km}$, and

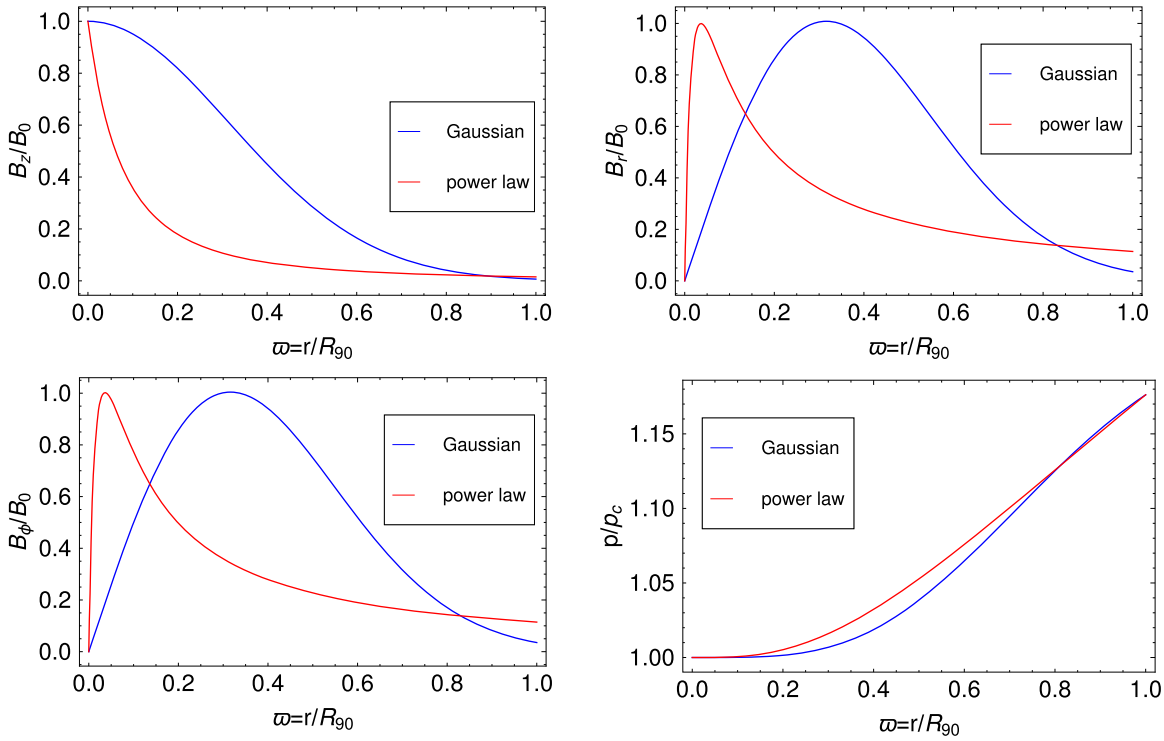

Figure 14. Radial distribution of the magnetic field components B_z, B_r, B_ϕ, and gas pressure p normalized with respect to the values at the flux tube center, B_0, p_c, for Gaussian and power-law shape functions for the parameter set of run *S*1 in Table 4. The horizontal axes are scaled with the total radius of the flux tube R and the values of the scale factors are $B_0 = 1$ kG and $p_c = 10^5$ dyne cm^{-2}.

$1\,\mathrm{kG} \leqslant B_0 \leqslant 1.5\,\mathrm{kG}$, the magnetic and thermodynamic quantities are in reasonable agreement with the solar atmosphere (Vernazza et al. 1981), which also validates the MBP size and magnetic field strength distribution (Utz et al. 2009, 2013). For the self-similar model, the radial sizes of the flux tubes depend on the choice of the dimensionless input parameters $\{\psi_b, \bar{f}, \bar{B'_{z0}}, \bar{\chi}\}$. In the domain of the selected parameter space (see Table 4), the maximum and minimum radii of the flux tubes are 678 and 151 km as obtained from the Gaussian model, whereas for the power-law model with $n_P = 3$, the maximum and minimum values of the radii are calculated to be 826 and 184 km, respectively, which are also in reasonable agreement with the observations of MBP size distribution by Utz et al. (2009).

3. For the Coulomb function model, we note that the value of α decreases with R (see Table 3), which lowers the poloidal current I_p and the twist of the field lines. The 3D geometries of the field lines for different twists are shown in Figures 6 and 7 for open and closed field Coulomb function models, respectively. In the self-similar model, the twist of the field lines increases with $\bar{\chi}$, as shown in Figures 12 and 13 for the Gaussian and power-law profiles, respectively, which follows from Equation (66).
4. The gas pressure for both the Coulomb function and self-similar models increases along the radial direction from the axis to the boundary (see Figures 14 and 17), whereas it decreases along the vertical height from the photosphere to the transition region (see Figures 18 and 19), which is similar to the result obtained by Shelyag et al. (2010) for MBPs, where the gas pressure inside the MBPs increases radially though the change is not significant, and decreases vertically. Gent et al. (2013, 2014) studied the cases of single and multiple flux tubes, where the internal gas pressure is nearly same along the radial distance but decreases with height. The density within the flux tube does not change radially but it decreases along z, for both Coulomb function and self-similar models (see Figures 9 and 16). Our model predicts that the atmosphere inside the flux tube is nearly plane-parallel, which is comparable to the model obtained for MBPs by Shelyag et al. (2010).
5. In the solar atmosphere, the temperature in the transition region rises perhaps because the shock dissipation of waves plays a dominant role, which is not included in our model. We have also not implemented the temperature profile by Vernazza et al. (1981) (VAL model); however, our model is self-consistent, obtained by solving the GSE without shock heating. Therefore, we do not see the drastic rise of the temperature with height. Our vertical simulation domain is restricted from the photosphere to the transition region in which our input external atmosphere model is valid. Both the flux tube models we built are non-isothermal, and the temperature increases along the radial direction for both Coulomb function open field and self-similar models (see Figures 17, 18, and 20). The vertical variation of the temperature is constant at the axis, but it increases with height away from the axis for the Coulomb function open field and self-similar models (see Figures 18 and 20).
6. Hewitt et al. (2014), Uitenbroek & Criscuoli (2013), and Riethmüller & Solanki (2017) reported the simulation results of MBPs using MuRAM and Copenhagen-Stagger code in which the obtained values of magnetic field strength, pressure, density, and temperature inside the flux tube are in reasonable agreement with our predictions.
7. The 2D simulations of the propagation of linear and nonlinear magnetoacoustic waves through an open magnetic

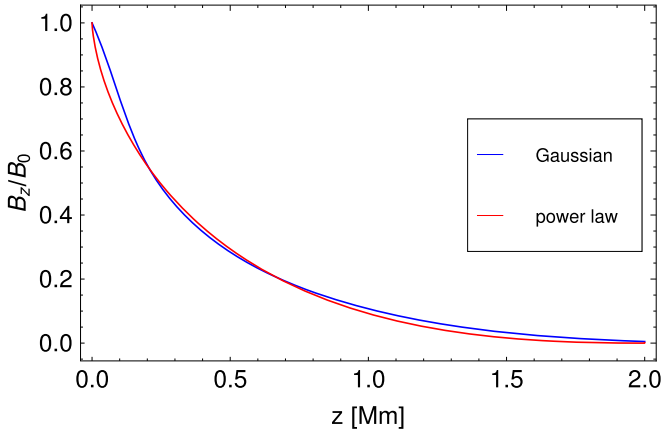

Figure 15. Vertical distribution of B_z at the axis of the flux tube, obtained from the self-similar model for the Gaussian and power-law profiles for the parameter set of run $S1$ in Table 4.

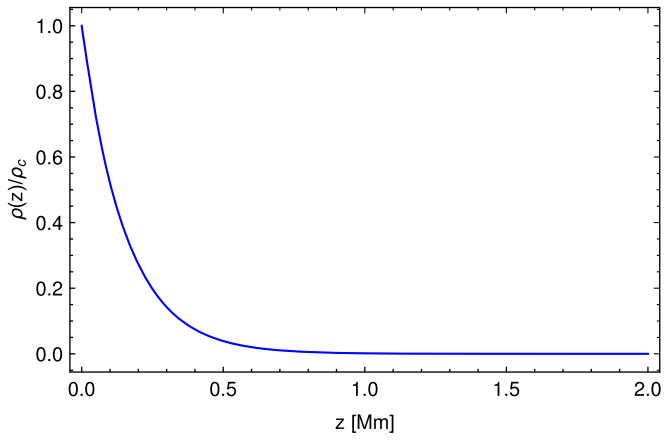

Figure 16. Vertical distribution of density, $\rho(z)$, obtained from the self-similar model for the parameter set of run $S1$ in Table 4, which is normalized with respect to $z = 0$ value, ρ_c, for both the Gaussian and power-law profiles. The horizontal axis is scaled in units of Mm. The value of scale factor $\rho_c = 2.37 \times 10^{-7}$ g cm^{-3}.

flux tube, embedded in the solar atmosphere from the photosphere to the corona, were carried out by Fedun et al. (2011). We can incorporate our solutions as the background condition for such numerical studies of waves and their kinematic properties by taking realistic inputs of the field strength and pressure distribution observed in the solar atmosphere.

8. The Coulomb function model gives both open and closed field flux tube solutions, which can be co-added to build a canopy structure. A cartoon diagram of the magnetic canopy is shown in Figure 21, where the closed field lines (red), Ψ_C^C, are present between the open field flux tubes and obtained from the Coulomb function, where the open field lines (blue), Ψ_C^O and Ψ_S^O, of the neighboring flux tubes merge with each other to form a canopy structure. This is similar to the structures assumed in the numerical simulations by Gent et al. (2014), constructed by a different self-similar flux tube solution. We can use our solutions for inputs to simulations to build such canopy structures. The self-similar flux tube model gives an open field structure of the flux tube that is embedded in a continuous magnetic medium and spans up to infinity in the radial direction. The magnetic and thermodynamic quantities we estimated from both Coulomb function and self-similar models are nearly similar, whereas there are some differences in the structures of the magnetic and thermodynamic profiles.

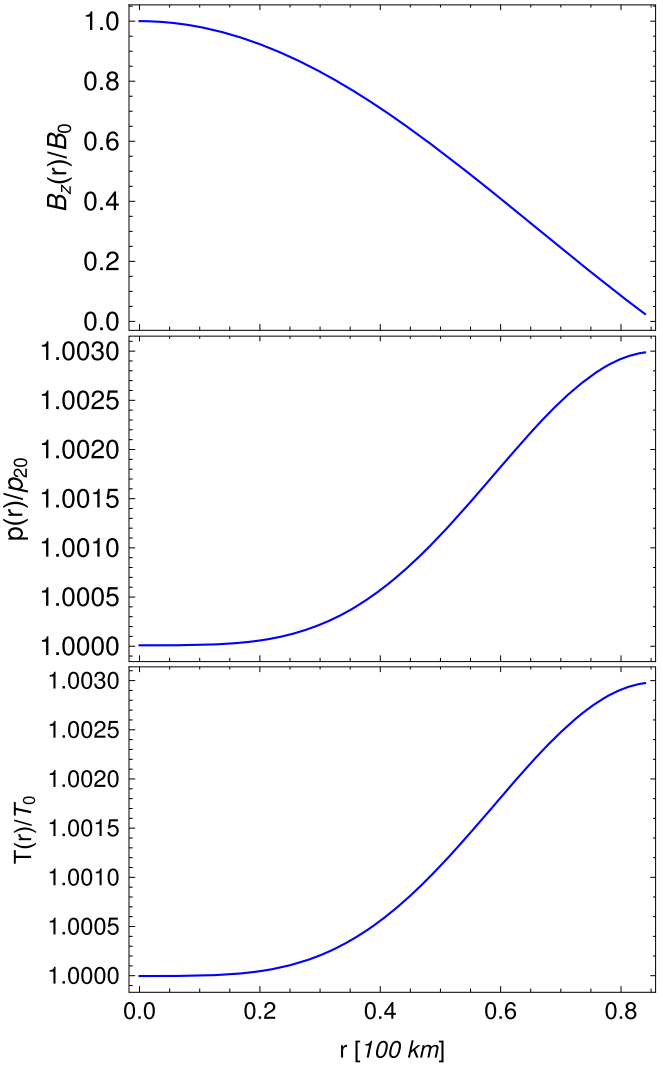

Figure 17. Vertical distribution of B_z, p, and T, normalized with respect to the values at the center of the flux tube, B_0, p_{20}, and T_0, respectively, from the axis of the flux tube to the MBP boundary for $r_b = 84$ km at $z = 0$, obtained from the Coulomb function open flux tube model for the parameter set of run $C4$ in Table 3. The horizontal axis is scaled in the units of 100 km and the values of the scale factors are $B_0 = 1$ kG, $p_{20} = 1.03 \times 10^5$ dyne cm^{-2} and $T_0 = 5656$ K.

More advanced observations of the magnetic and thermodynamic structures of the MBPs will provide a better selection of parameter inputs to discriminate between our models.

8. Summary and Conclusions

In this work, we have constructed two different models of flux tubes with twisted magnetic fields, the Coulomb function helical flux tube model and the self-similar model, by solving GSE semianalytically. We tabulate the expressions of the magnetic and thermodynamic functions for the Coulomb and self-similar models in Table 6, and highlight the novel features of this work as follows:

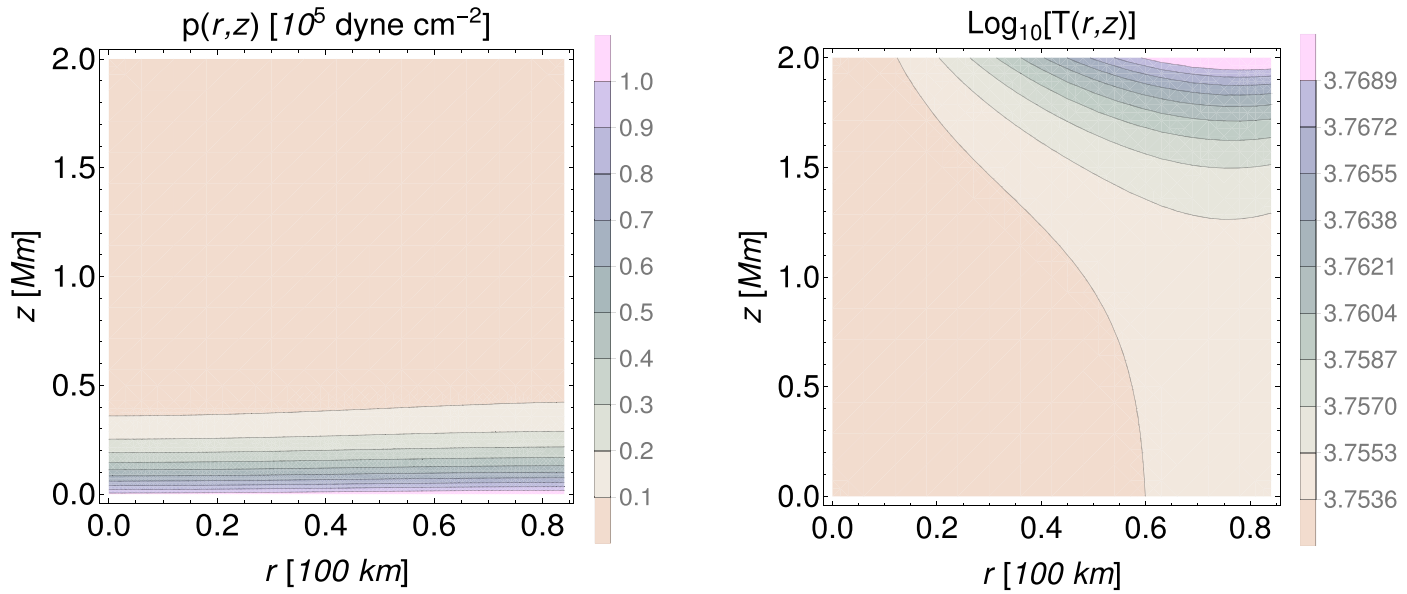

Figure 18. The 2D variation of p (left) and T (right) in the $r - z$ plane for $r_b = 84$ km obtained from the Coulomb function model for the parameter set of run $C4$ in Table 3. The horizontal axes are scaled in the of 100 km and the vertical axes are scaled in units of Mm.

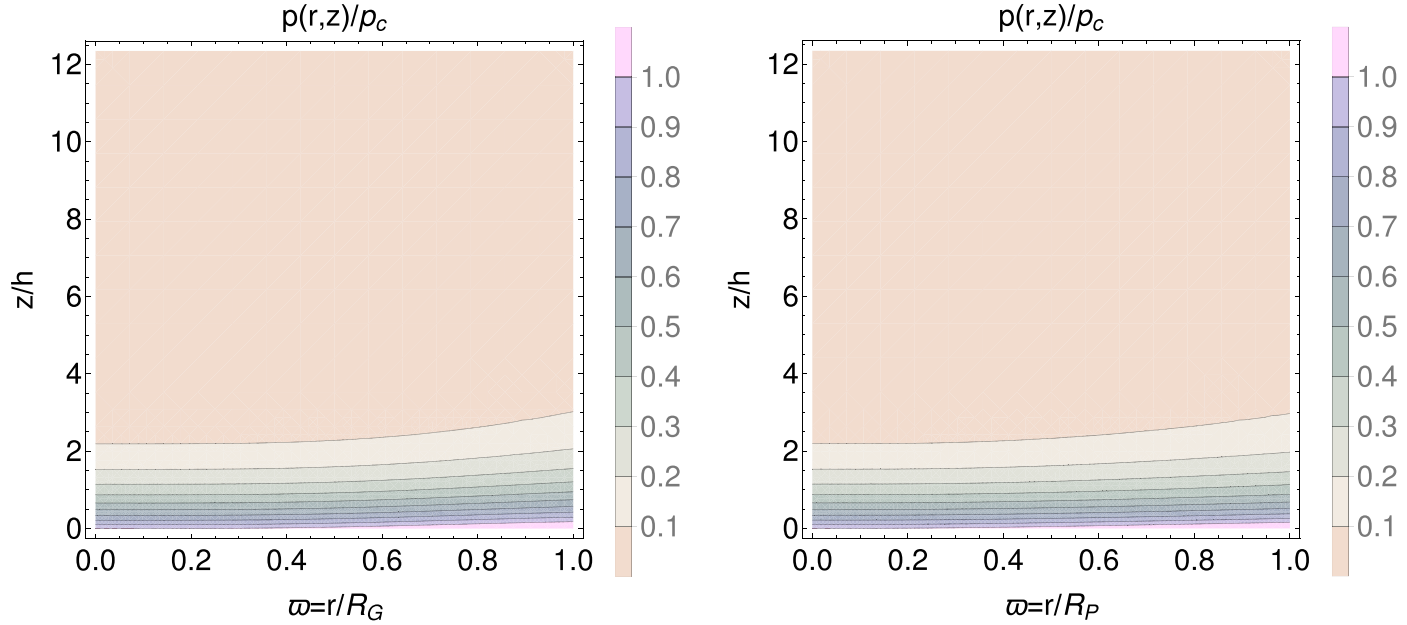

Figure 19. The 2D variation of p in the $r - z$ plane obtained from the self-similar model for the Gaussian (left) and power-law (right) profiles with $n_P = 3$, for the parameter set of run $S1$ in Table 4. The horizontal axes are scaled with total radii $R_G = 150$ and $R_P = 130$ km, and the vertical axes are scaled with pressure-scale height, $h = 162$ km.

1. By incorporating the form of gas pressure and poloidal current we have solved GSE to obtain the flux function for the Coulomb function model. The solution of the Coulomb function model is the combination of a homogeneous part and a particular part. The homogeneous part with closed geometry is separable with a Coulomb function in r, whereas the z-part decreases exponentially with height, and the particular part with open geometry is a power series of r that is independent of z.
2. Using appropriate BCs and employing the presence of the sheet current at the boundary of the flux tube, we have determined the parameters $a(R)$, $\alpha(R)$, $\kappa(R)$, $b(R, B_0)$, $\psi_b(R, B_0)$ and $\bar{p}(R, B_0)$ in terms of the input parameters $\{R, B_0\}$, which are the free parameters in the model, and k is calculated from the pressure values at the photosphere and transition region obtained from Avrett & Loeser (2008) model. The values of the parameters for the Coulomb function model are listed in Table 3.
3. In the Coulomb function model, the solution consisting of homogeneous and particular parts together represents an open field flux tube solution, where the field lines rise from the photosphere. The homogeneous solution depicts a closed field flux tube model, which is discussed in SM18. The values of the magnetic field strength and thermodynamic quantities inside the flux tube are calculated and are summarized in Table 5. 3D visualizations of both the open and closed field lines are shown in Figures 6 and 7 for the parameter sets of runs $C4$ and $C10$ corresponding to Table 3.

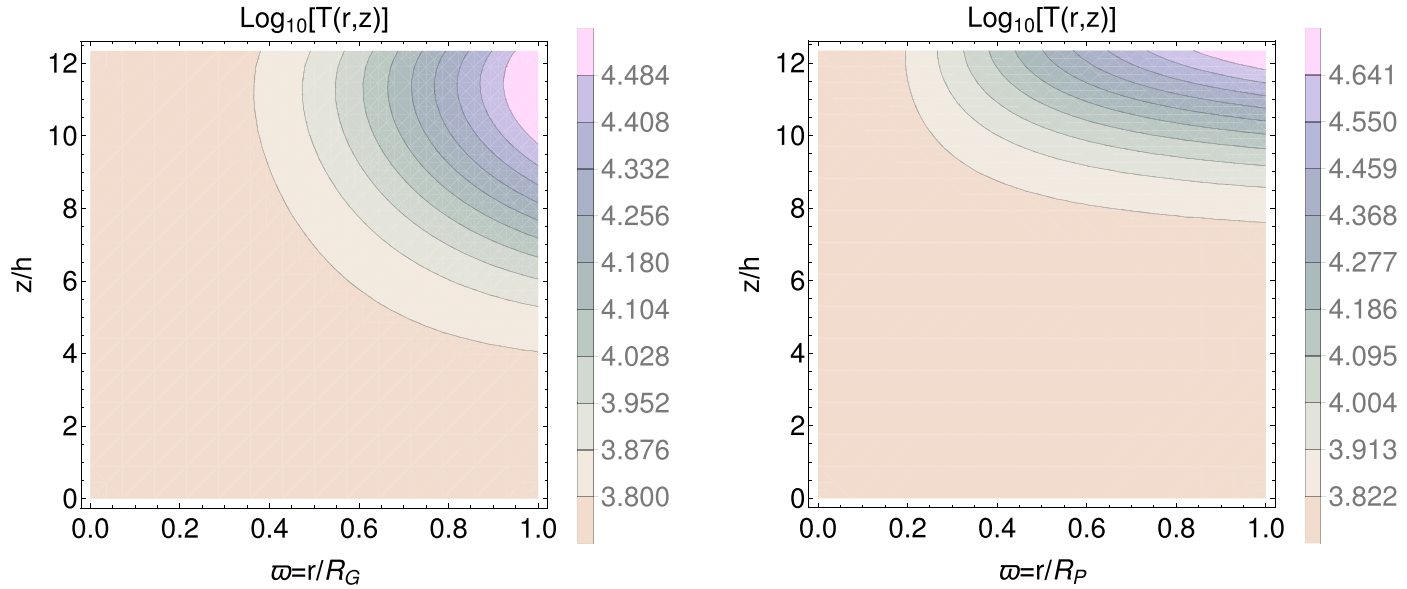

Figure 20. The 2D variation of T in the $r - z$ plane for the Gaussian (left) and power-law (right) profiles with $n_P = 3$ obtained from the self-similar model for the parameter set $S1$ in Table 4. The horizontal axes are scaled with total radii $R_G = 150$ km and $R_P = 130$ km, and the vertical axes are scaled with pressure-scale height, $h = 162$ km.

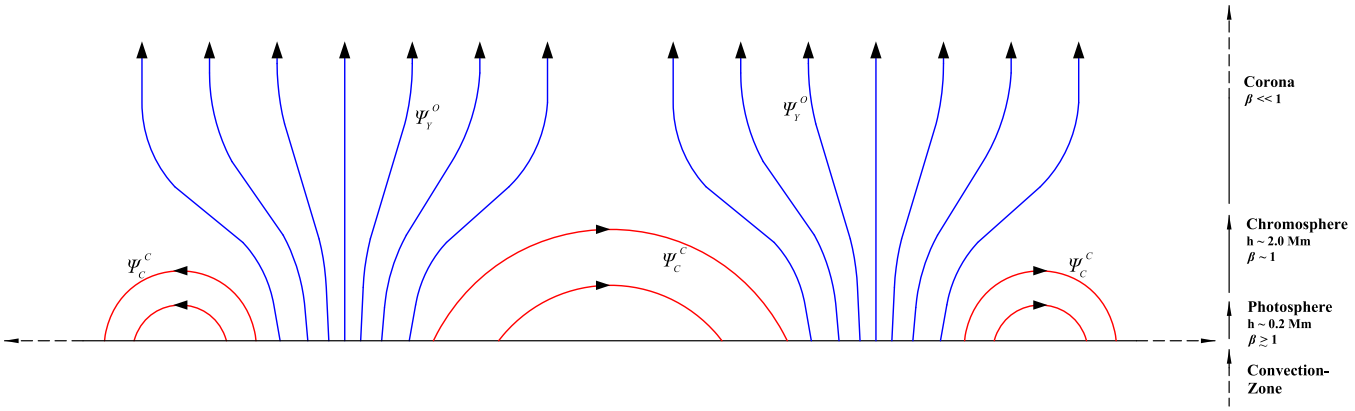

Figure 21. Cartoon diagram of magnetic canopy structure, where the closed field lines (red), which are obtained by the Coulomb function closed field solution, Ψ_C^C, rise and fall back in the photosphere, present between two open field flux tubes. The open field lines (blue), obtained by the Coulomb function open field and self-similar solution, Ψ_Y^O ($Y = C$, for Coulomb function, and $Y = S$, for self-similar models), of two neighboring flux tubes merge together to form magnetic canopy structure (An improvised version of the illustration in Judge 2006).

4. In the self-similar model, we have employed an extra term, $p_c \exp(-2kz)$, with p_1 in Equation (55), to maintain the hydrostatic pressure balance under the influence of stratified solar gravity, and taken two options for the shape functions: $D_X(\xi)$ from Equation (57), which is the extension of previous models by ST58, Yun (1971), and Osherovitch (1979, 1982). We have incorporated the resulting two different shape functions, generalized Gaussian and power-law profiles, to obtain open field flux tube solutions. We have taken a range of the parameters, Ψ_b, B_0, p_c, B'_{z0}, and χ (see Table 4), that is consistent with the solar atmosphere, to study the structure and the properties of the flux tubes. The size of the flux tubes and the magnitude of the thermodynamic and magnetic field strengths depend on the choice of the input parameters, but the magnetic and thermodynamic structures remain similar. We have calculated the magnetic field strength and the thermodynamic quantities inside the flux tube. These are given in Table 5, for the parameter set of run $S1$ corresponding to Table 4.
5. Preliminary calculations using the constraint of relative helicity based on the formulations given in Prasad et al. (2014) and Prasad & Mangalam (2016), and applying the constrained energy minimization principle (Taylor 1974; Finn & Antonsen 1983; Mangalam & Krishan 2000), indicate that stable configurations are possible for some regions in the parameter space of $\{B_0, R\}$. We plan a complete solution of this allowed region and test it with numerical simulations in a paper in preparation.

The flux tube models presented here give useful estimates of the magnitude and the distribution of the magnetic field strength and thermodynamic quantities, from the photosphere to the transition region, that can be verified by future observations. Work on self-similar closed and twisted field structure is in progress. The solutions we obtained for different flux tubes can be used for the dynamical simulation of wave propagation through the flux tubes, which is important for studying coronal heating by waves.

Table 6
Formularies of Different Functions Obtained for the Coulomb Function Helical Flux Tube and Self-similar Model

Functions	Formulae for the Coulomb Function Model
$s(\varpi)$	$c(F_0(-\alpha-\kappa^2,\sqrt{a}\,\varpi^2)+F_0^*(-\alpha-\kappa^2,\sqrt{a}\,\varpi^2)$
$Z(\bar{z})$	$\exp\left(-\frac{2\sqrt{2}\,\kappa a^{1/4}\bar{z}}{\tau}\right)$
$\psi_p(\varpi)$	$\frac{i\sqrt{a}b\varpi^2}{4\psi_b}\left[e^{i\sqrt{a}\varpi^2}\sum_{n=0}^{\infty}\frac{F_2^1\left(n+2,1;n+2-i\alpha;\frac{1}{2}\right)(-i\sqrt{a}\varpi^2)^n}{(n+1-i\alpha)n!}-e^{-i\sqrt{a}\varpi^2}\sum_{n=0}^{\infty}\frac{F_2^1\left(n+2,1;n+2+i\alpha;\frac{1}{2}\right)(i\sqrt{a}\varpi^2)^n}{(n+1+i\alpha)n!}\right]$
$\psi_C(\varpi,\bar{z})$	$s(\varpi)Z(\bar{z})+\psi_p(\varpi)$
$B_r(\varpi,\bar{z})$	$\frac{B_0\sqrt{2}\psi_b\kappa}{a^{1/4}}s(\varpi)Z(\bar{z})$
$B_z(\varpi,\bar{z})$	$\frac{B_0\psi_b}{2\sqrt{a}\varpi}[s'(\varpi)Z(\bar{z})+\psi_p'(\varpi)]$
$B_\phi(\varpi,\bar{z})$	$\frac{B_0\sqrt{2}\alpha^{1/2}\psi_b}{a^{1/4}}[s(\varpi)Z(\bar{z})+\psi_p(\varpi)]$
$p(\varpi,\bar{z})$	$B_0^2\left[\left(\frac{\psi_b^2 s^2(\varpi)}{8\pi}+\bar{p}_{20}\right)Z^2(\bar{z})+\left(\frac{\psi_b^2 s(\varpi)\psi_p(\varpi)}{4\pi}+\frac{b\psi_b s(\varpi)}{2\sqrt{2a}}\right)Z(\bar{z})+\left(\frac{\psi_b^2\psi_p^2}{8\pi}+\frac{b\psi_b\psi_p}{2\sqrt{2a}}\right)\right]$
$\rho(\bar{z})$	$\frac{4\sqrt{2}\,\kappa a^{1/4}p_{20}}{gR}Z^2(\bar{z})$
$T(\varpi,\bar{z})$	$\frac{\bar{\mu}B_0^2 gR}{4\sqrt{2}R_g\kappa a^{1/4}p_{20}}\left[\left(\frac{\psi_b^2 s^2(\varpi)}{8\pi}+\bar{p}_{20}\right)+\left(\frac{\psi_b^2 s(\varpi)\psi_p(\varpi)}{4\pi}+\frac{b\psi_b s(\varpi)}{2\sqrt{2a}}\right)\frac{1}{Z(\bar{z})}+\left(\frac{\psi_b^2\psi_p^2}{8\pi}+\frac{b\psi_b\psi_p}{2\sqrt{2a}}\right)\frac{1}{Z^2(\bar{z})}\right]$
Functions	**Formulae for the Self-similar Model**
$\xi(\varpi,\bar{z})$	$\sqrt{\frac{\tau}{\psi_b D_0}}\varpi y(\bar{z})$
$\psi_G(\varpi,\bar{z})$	$1-\frac{\Gamma(2/n_G,\xi^{n_G})}{\Gamma(2/n_G)};\quad (n_G>0)$
$\psi_P(\varpi,\bar{z})$	$1-(1+\xi)^{1-n_P}(1+\xi(n_P-1));\quad (n_P>2)$
$B_r(\varpi,\bar{z})$	$-\frac{B_0\varpi}{D_0}y(\bar{z})y'(\bar{z})D_X(\xi)$
$B_z(r,z)$	$\frac{B_0}{D_0}y^2(z)D_X(\xi)$
$B_\phi(\varpi,\bar{z})$	$\frac{\sqrt{\bar{\chi}}B_0}{D_0}\varpi y^2(\bar{z})D_X(\xi)$
$p(\varpi,\bar{z})$	$B_0^2\left[\frac{\bar{J}}{2}\psi^2+\bar{p}_c e^{-2\bar{k}\bar{z}}\right]$
$\rho(\bar{z})$	$\frac{2\bar{k}\bar{z}\bar{p}_c B_0^2}{gz_0}e^{-2\bar{k}\bar{z}}$
$T(\varpi,\bar{z})$	$\frac{\bar{\mu}gz_0}{2R_g\bar{k}\bar{z}\bar{p}_c}\left(\frac{\bar{J}}{2}\psi^2 e^{2\bar{k}\bar{z}}+\bar{p}_c\right)$

Note. Here, $s(\varpi)$, $Z(\bar{z})$, and $\psi_p(\varpi)$ are given by Equations (18), (19), (23), and $\bar{p}_{20}=p_{20}/B_0^2$. ξ is a self-similar parameter in which $y(\bar{z})$ is obtained by solving Equation (60) and $\bar{p}_0=p_0/B_0^2$, $\bar{p}_c=p_c/B_0^2$, $\bar{k}=kz_0$. The value of the constants are $\bar{\mu}=1.12$, $g=2.74\times10^4$ cm s^{-2}, $k=3.4\times10^{-8}$ cm^{-1}, and $z_0=10^8$ cm.

We thank V. Fedun, R. Erdélyi, and S. Shelyag for useful discussions. We thank the anonymous referee for insightful comments and helpful suggestions. We also thank the support staff of the IIA HPC facility, VBO (IIA, Kavalur) staff for their hospitality during our visits, and Saikat Das for help with Figures 2 and 21.

Appendix A
Derivation of the Explicit form of B_z for the Coulomb Function Model

The homogeneous solution $s(\varpi)$ which is given by the Equation (18), can be represented in terms of the Whittaker–M function (SM18), where the Whittaker–M function can be expressed in terms of the hypergeometric function by the standard relation (Dixit & Moll 2015)

$$M_{t,m}(\nu)=e^{-\nu/2}\nu^{m+\frac{1}{2}}F_1^1\left(\frac{1}{2}+m-t,\,1+2\,m,\,\nu\right),\qquad(74)$$

where F_1^1 represents the hypergeometric function with the arguments t, m, and ν. Taking the real part of $\psi_h(\varpi,\bar{z})$ from Equation (20) and $\psi_p(\varpi)$ from (23), and using Equations ((24), (74)) we obtain

$$\begin{aligned}B_z(\varpi,\bar{z})=&B_0\psi_b c\exp\left(-\frac{2\sqrt{2}\,\kappa a^{1/4}\bar{z}}{\tau}\right)\\&\times[8(1+i\sqrt{a}\,\varpi^2)F_1^1(1+i\alpha,2,2i\sqrt{a}\,\varpi^2)\\&-8\sqrt{a}\,\varpi^2F_1^1(1+i\alpha,3,2i\sqrt{a}\,\varpi^2)]\\&+\frac{B_0\psi_b}{2\sqrt{a}}\left(\frac{\psi_p'(\varpi)+\psi_p'^*(\varpi)}{2\varpi}\right)\end{aligned}\qquad(75)$$

where, $B_0\equiv B_z(0,0)$, and from Equation (75) we obtain,

$$1=8\psi_b c+\frac{\psi_b}{2\sqrt{a}}\left[\frac{\psi_p'(\varpi)+\psi_p'^*(\varpi)}{2\varpi}\right]_{\varpi=0},\qquad(76)$$

where the identity $F_1^1(1+i\alpha,2,0)=1$ is applied. By expanding the last term on the RHS of Equation (76), we obtain

$$\begin{aligned}1=8\psi_b c+\frac{ib}{2}\Bigg[&\frac{F_2^1(1,-i\alpha,2-i\alpha,-1)}{1-i\alpha}\\&-\frac{F_2^1(1,i\alpha,2+i\alpha,-1)}{1+i\alpha}\Bigg]\end{aligned}\qquad(77)$$

and the expression for c is given by

$$\begin{aligned}c=\frac{1}{8\psi_b}\Bigg[1-\frac{ib}{2}\Bigg(&\frac{F_2^1(1,-i\alpha,2-i\alpha,-1)}{1-i\alpha}\\&-\frac{F_2^1(1,i\alpha,2+i\alpha,-1)}{1+i\alpha}\Bigg)\Bigg].\end{aligned}\qquad(78)$$

Hence, from Equation (75), we obtain the explicit form for $B_z(\varpi,\bar{z})$ that is given in Equation (25).

Appendix B
Explicit Forms of the BCs for Coulomb Function Model

The explicit forms of Equations 44(a)–44(e) are

$$F_0(-\alpha-\kappa^2,\sqrt{a})+F_0^*(-\alpha-\kappa^2,\sqrt{a})=0, \tag{79}$$

$$\left[\frac{1}{\varpi^2}\frac{d}{d\varpi}\left(\varpi^2 e^{i\sqrt{a}\varpi^2}\sum_{n=0}^{\infty}\frac{F_2^1(n+2,1,n+2-i\alpha,1/2)(-i\sqrt{a}\varpi^2)^n}{(n+1-i\alpha)n!}-\varpi^2 e^{-i\sqrt{a}\varpi^2}\sum_{n=0}^{\infty}\frac{F_2^1(n+2,1,n+2+i\alpha,1/2)(i\sqrt{a}\varpi^2)^n}{(n+1+i\alpha)n!}\right)\right]_{\varpi=1}=0, \tag{80}$$

$$\left[1-\frac{ib}{2}\left(\frac{F_2^1(1,-i\alpha,2-i\alpha,-1)}{1-i\alpha}-\frac{F_2^1(1,i\alpha,2+i\alpha,-1)}{1=i\alpha}\right)\right]^2\cdot\left(\frac{d}{d\varpi}[F_0(\alpha-\kappa^2,\sqrt{a}\varpi^2)+F_0^*(\alpha-\kappa^2,\sqrt{a}\varpi^2)]_{\varpi=1}\right)^2=\bar{p}a, \tag{81}$$

$$b=-\frac{\psi_b}{2}\left(1+\frac{6\alpha}{\sqrt{a}}\right), \tag{82}$$

$$\int_0^1\left[e^{-2\kappa_t}\left(1-\frac{ib}{2}\left[\frac{F_2^1(1,-i\alpha,2-i\alpha,-1)}{1-i\alpha}-\frac{F_2^1(1,i\alpha,2+i\alpha,-1)}{1+i\alpha}\right]\right)^2\cdot(F_0(-\alpha-\kappa^2,\sqrt{a}\varpi^2)+F_0^*(-\alpha-\kappa^2,\sqrt{a}\varpi^2))^2+8e^{-\kappa_t}\psi_b\left(\psi_p+\psi_p^*+\frac{2b}{\psi_b}\right)\cdot\left(1-\frac{ib}{2}\left[\frac{F_2^1(1,-i\alpha,2-i\alpha,-1)}{1-\alpha}-\frac{F_2^1(1,i\alpha,2+i\alpha,-1)}{1+\alpha}\right]\right)^2\cdot(F_0(-\alpha-\kappa^2,\sqrt{a}\varpi^2)+F_0^*(-\alpha-\kappa^2,\sqrt{a}\varpi^2))+\frac{\psi_b^2}{4}(\psi_p+\psi_p^*)^2+b\psi_b(\psi_p+\psi_p^*)\right]d\varpi=\bar{p} \tag{83}$$

respectively, where, $\psi_p(\varpi)$ is given by Equation (23), $\kappa_t=kz_t$, and $\psi_p(\varpi=1)=\psi_b$.

ORCID iDs

Samrat Sen https://orcid.org/0000-0003-1546-381X
A. Mangalam https://orcid.org/0000-0001-9282-0011

References

Abramowitz, M., & Stegun, I. A. 1972, Handbook of Mathematical Functions with Formulas, Graphs, and Mathematical Tables (New York: Dover)
Aschwanden, M. J., Nightingale, R. W., & Alexander, D. 2000, ApJ, 541, 1059
Atanasiu, C. V., Günter, S., Lackner, K., & Miron, I. G. 2004, PhPl, 11, 3510
Avrett, E. H., & Loeser, R. 2008, ApJS, 175, 229
Balthasar, H., & Schmidt, W. 1993, A&A, 279, 243
Berger, T. E., Schrijver, C. J., Shine, R. A., et al. 1995, ApJ, 454, 531
Centeno, R., Socas-Navarro, H., Lites, B., et al. 2007, ApJL, 666, L137
Dixit, A., & Moll, V. 2015, Scientia Series A, 26, 49, http://scientia.mat.utfsm.cl/vol26.html
Fedun, V., Erdélyi, R., & Shelyag, S. 2009, SoPh, 258, 219
Fedun, V., Verth, G., Jess, D. B., & Erdélyi, R. 2011, ApJL, 740, L46
Finn, J. M., & Antonsen, T. M., Jr. 1983, PhFl, 26, 3540
Gent, F. A., Fedun, V., & Erdélyi, R. 2014, ApJ, 789, 42
Gent, F. A., Fedun, V., Mumford, S. J., & Erdélyi, R. 2013, MNRAS, 435, 689
Grad, H., & Rubin, H. 1958, in Int. Conf. Peaceful Uses of Atomic Energy 31, Hydromagnetic Equlibria and Force-Free Fields, ed. J. H. Martens et al. (Geneva: U.S. Government Printing Office), 190
Guglielmino, S. L., Pillet, V. M., del Toro Iniesta, J. C., et al. 2011, in IAU Symp. 274, Advances in Plasma Astrophysics, ed. A. Bonanno, E. de Gouveia Dal Pino, & A. G. Kosovichev (Cambridge: Cambridge Univ. Press), 140
Hagenaar, H. J., Schrijver, C. J., Title, A. M., & Shine, R. A. 1999, ApJ, 511, 932
Hewitt, R. L., Shelyag, S., Mathioudakis, M., & Keenan, F. P. 2014, A&A, 565, A84
Judge, P. 2006, in ASP Conf. Ser. 354, Solar MHD Theory and Observations: A High Spatial Resolution Perspective, ed. J. Leibacher, R. F. Stein, & H. Uitenbroek (San Francisco, CA: ASP), 259
Lagg, A., Solanki, S. K., Riethmüller, T. L., et al. 2010, ApJL, 723, L164
Mangalam, A., & Krishan, V. 2000, JApA, 21, 299
Muller, R., & Mena, B. 1987, SoPh, 112, 295
Muller, R., Roudier, T., Vigneau, J., & Auffret, H. 1994, A&A, 283, 232
Murawski, K., Solov'ev, A., Musielak, Z. E., Srivastava, A. K., & Kraśkiewicz, J. 2015, A&A, 577, A126
Osherovitch, V. A. 1979, SoPh, 64, 261
Osherovitch, V. A. 1982, SoPh, 77, 63
Pahlke, K.-D., & Wiehr, E. 1990, A&A, 228, 246
Parker, E. N. 1988, ApJ, 330, 474
Peter, H., Gudiksen, B. V., & Nordlund, A. 2005, in ESA Special Publication 596, Chromospheric and Coronal Magnetic Fields, ed. D. E. Innes, A. Lagg, & S. A. Solanki (Noordwijk: ESA), 14.1
Prasad, A., & Mangalam, A. 2016, ApJ, 817, 12
Prasad, A., Mangalam, A., & Ravindra, B. 2014, ApJ, 786, 81
Riethmüller, T. L., & Solanki, S. K. 2017, A&A, 598, A123
Ruzmaikin, A., & Berger, M. A. 1998, A&A, 337, L9
Schlüter, A., & Temesváry, S. 1958, in IAU Symp. 6, The Internal Constitution of Sunspots, ed. B. Lehnert (Cambridge: Cambridge Univ. Press), 263
Sen, S., & Mangalam, A. 2018, AdSpR, 61, 617
Shafranov, V. 1958, Journal of Theoretical and Experimental Physics, 33, 710, http://www.jetp.ac.ru/cgi-bin/e/index/e/6/3/p545?a=list
Shelyag, S., Mathioudakis, M., Keenan, F. P., & Jess, D. B. 2010, A&A, 515, A107
Solov'ev, A. A., & Kirichek, E. A. 2015, AstL, 41, 211
Solov'ev, L. 1968, Journal of Experimental and Theoretical Physics, 26, 626, http://www.jetp.ac.ru/cgi-bin/e/index/e/26/6/p1167?a=list
Srivastava, A. K., Shetye, J., Murawski, K., et al. 2017, NatSR, 7, 43147
Steiner, O., Pneuman, G. W., & Stenflo, J. O. 1986, A&A, 170, 126
Stepanov, V. E. 1965, in IAU Symp. 22, Stellar and Solar Magnetic Fields, ed. R. Lust (Amsterdam: North-Holland Pub. Co), 267
Taylor, J. B. 1974, PhRvL, 33, 1139
Thalmann, J. K., Tiwari, S. K., & Wiegelmann, T. 2013, ApJ, 769, 59
Uitenbroek, H., & Criscuoli, S. 2013, MmSAI, 84, 369
Utz, D., Hanslmeier, A., Möstl, C., et al. 2009, A&A, 498, 289
Utz, D., Jurčák, J., Hanslmeier, A., et al. 2013, A&A, 554, A65
van Ballegooijen, A. A. 1986, ApJ, 311, 1001
Vernazza, J. E., Avrett, E. H., & Loeser, R. 1981, ApJS, 45, 635
Vigeesh, G., Hasan, S. S., & Steiner, O. 2009, A&A, 508, 951
Wittmann, A. 1974, SoPh, 36, 29
Yang, Y., Li, Q., Ji, K., et al. 2016, SoPh, 291, 1089
Yun, H. S. 1971, SoPh, 16, 398
Zhang, H., Scharmer, G., Lofdahl, M., & Yi, Z. 1998, SoPh, 183, 283